Extragalactic background light : a measurement at 400 nm using dark cloud shadow - II. Spectroscopic separation of the dark cloud's light, and results

Mattila, K.

2017-09

Mattila , K , Väisänen , P , Lehtinen , K , von Appen-Schnur , G & Leinert , C 2017 , ' Extragalactic background light : a measurement at 400 nm using dark cloud shadow - II. Spectroscopic separation of the dark cloud's light, and results ' , Monthly Notices of the Royal Astronomical Society , vol. 470 , no. 2 , pp. 2152-2169 . https://doi.org/10.1093/mnras/stx1296

http://hdl.handle.net/10138/215212
https://doi.org/10.1093/mnras/stx1296

unspecified
publishedVersion

Monthly Notices of the ROYAL ASTRONOMICAL SOCIETY

MNRAS **470,** 2152–2169 (2017) doi:10.1093/mnras/stx1296
Advance Access publication 2017 May 25

Extragalactic background light: a measurement at 400 nm using dark cloud shadow – II. Spectroscopic separation of the dark cloud's light, and results*

K. Mattila,[1]† P. Väisänen,[2,3]† K. Lehtinen,[1] G. von Appen-Schnur[4] and Ch. Leinert[5]

[1]*Department of Physics, University of Helsinki, PO Box 64, FI-00014 Helsinki, Finland*
[2]*South African Astronomical Observatory, PO Box 9 Observatory 7935, Cape Town, South Africa*
[3]*Southern African Large Telescope, PO Box 9 Observatory 7935, Cape Town, South Africa*
[4]*Astronomisches Institut, Ruhr-Universität Bochum, Universitätsstrasse 150, D-44801 Bochum, Germany*
[5]*Max-Planck-Institut für Astronomie, Königstuhl 17, D-69117 Heidelberg, Germany*

Accepted 2017 May 23. Received 2017 April 28; in original form 2017 February 15

ABSTRACT

In a project aimed at measuring the optical extragalactic background light (EBL), we are using the shadow of a dark cloud. We have performed, with the ESO VLT/FORS, spectrophotometry of the surface brightness towards the high-galactic-latitude dark cloud Lynds 1642. A spectrum representing the difference between the opaque core of the cloud and several unobscured positions around the cloud was presented in Paper I. The topic of this paper is the separation of the scattered starlight from the dark cloud itself which is the only remaining foreground component in this difference. While the scattered starlight spectrum has the characteristic Fraunhofer lines and the discontinuity at 400 nm, typical of integrated light of galaxies, the EBL spectrum is a smooth one without these features. As template for the scattered starlight, we make use of the spectra at two semitransparent positions. The resulting EBL intensity at 400 nm is $I_{\rm EBL} = 2.9 \pm 1.1\ 10^{-9}$ erg cm^{-2} s^{-1} sr^{-1} Å^{-1} or 11.6 ± 4.4 nW m^{-2}sr^{-1}, which represents a 2.6σ detection; the scaling uncertainty is +20 per cent/−16 per cent. At 520 nm, we have set a 2σ upper limit of $I_{\rm EBL} \leq 4.5\ 10^{-9}$ erg cm^{-2} s^{-1} sr^{-1} Å^{-1} or ≤ 23.4 nW m^{-2}sr^{-1} +20 per cent/−16 per cent. Our EBL value at 400 nm is $\gtrsim 2$ times as high as the integrated light of galaxies. No known diffuse light sources, such as light from Milky Way halo, intra-cluster or intra-group stars appear capable of explaining the observed EBL excess over the integrated light of galaxies.

Key words: ISM: clouds – dust, extinction – solar neighbourhood – diffuse radiation – cosmology: observations.

1 INTRODUCTION

Besides the cosmic microwave background (CMB) also 'the other' extragalactic background radiations from γ- and X-rays over ultraviolet (UV), optical, near-infrared (NIR) to far-infrared (FIR) radiation and long radio waves have been recognized as an important source of information for cosmology and galaxy formation studies and have been intensively studied by both ground-based and space-borne telescopes; for a review, see e.g. Longair (1995). Energetically, the optical–NIR and the FIR components are (after the CMB) the most important ones. The source of energy for both of them is mainly the starlight, the direct one in optical–NIR and the dust-processed one in the mid- and far-IR. While already Loys de Chéseaux (1744) and Olbers (1823) recognized the relevance of the night sky darkness for cosmology, the optical EBL has remained, paradoxically, the observationally least well-determined component so far. This is the consequence of the smallness of the extragalactic background light (EBL) as compared to the much brighter sky foreground components.

The conventional approach for EBL measurement has been to observe the total sky brightness and try to measure or model all the foreground components. Then, after subtraction, what is left over is the EBL. In this method, because of smallness of the EBL, the two large surface brightness components, $I_{\rm total}$ and $I_{\rm foreground}$, must be very accurately known and, if measured by different telescopes or methods, *absolutely* calibrated at <0.5 per cent accuracy which for surface brightness measurements is hardly possible (Bernstein 2007).

When all or part of the observations are done from ground, the first hindrance is the atmospheric diffuse light (ADL), consisting of the Airglow (AGL), and the tropospheric scattered light. The

* KM, PV, KL and ChL dedicate this paper to the memory of Gerhard von Appen-Schnur, friend and colleague, who deceased on 2013 February 13.
† E-mail: mattila@cc.helsinki.fi (KM); petri@saao.ac.za (PV)

second large foreground is the zodiacal light (ZL), which remains a problem with full weight even if the observations are carried out outside the atmosphere. A very promising approach is to make the measurements beyond the interplanetary dust cloud. However, unless a small and accurately positioned aperture can be used, the light from stars in the measuring aperture enters with full weight and overwhelms the EBL (Matsuoka et al. 2011). Even if all these nearby foregrounds had been successfully determined, there remains, for an observer within the Galactic dust layer, the emission by interstellar gas and the diffuse galactic light (DGL), the starlight scattered by interstellar dust. No perfect cosmological windows, completely free of gas and dust, are known to exist. Besides the acronyms EBL, ADL, AGL, DGL and ZL we will in the following use also ISRF for interstellar radiation field, ISL for integrated starlight and IGL for the integrated light of galaxies.

In this paper, based on the results of Mattila et al. (2017), hereafter Paper I, we present a (spectro)photometric determination of the EBL using the dark cloud shadow method (Mattila 1976; Mattila 1990). The method utilizes the screening effect of a dark cloud on the background light. In this method, no absolute measurements or modelling of $I_{\rm total}$ and $I_{\rm foreground}$ are required. The difference of the night sky brightness in the direction of an opaque high-galactic-latitude dark cloud and a surrounding transparent area is due to two components only: (i) the EBL and (ii) the starlight that has been diffusely scattered by interstellar dust in the cloud. The three large foreground components, i.e. the ZL, the AGL and the tropospheric scattered light, are eliminated. Also any emission by interstellar gas or dust that is homogeneously distributed in front of the cloud is eliminated. A sketch shown as fig. 1 of Paper I illustrates the principle of the method. The method utilizes one and the same instrument for all sky components and, therefore, does not require any higher-than-usual calibration accuracy.

The main task in the method is to account for the surface brightness of the dark cloud. For the cloud, and even for its dark core, we have to take into account a substantial scattered light component. Such a component, although maybe smaller, is present in any direct photometric EBL measurement and is not an extra annoyance specific to the dark cloud method only. For efficient detection of the EBL with the dark cloud method it is essential that the dark cloud has an opaque core, $\tau > 10$, and that there are areas with good transparency in its immediate neighbourhood on sky.

The rest of this paper is organized as follows. In Section 2 the method of spectroscopic separation of the EBL from the scattered light is described. In Section 3 we present our observational results and error estimates for the EBL intensity in the blue band, $\lambda \sim 400$ nm, and at 520 nm. In Section 4 we discuss our EBL result in comparison with the IGL (as derived from deep galaxy counts) and with the γ-ray attenuation measurements of blazars. In the final Section 5, we present our summary and conclusions.

The paper has two appendices containing supporting data. Appendix A describes synthetic spectrum modelling of the Solar neighbourhood ISL; it is used for comparison with the empirically determined scattered light spectrum in the cloud. Appendix B presents a survey of possible sources of diffuse light from outskirts of galaxies, low surface brightness galaxies and intergalactic stars that could contribute substantially to the EBL

2 SEPARATION OF THE EBL AND SCATTERED LIGHT

The observational result of Paper I consists of the surface brightness spectra at the opaque central position, Pos8, and the semi-transparent positions 9 and 42 in L 1642 relative to the OFF positions: $\Delta I^0(\lambda)$(Pos8–OFF), $\Delta I^0(\lambda)$(Pos9 – OFF) and $\Delta I^0(\lambda)$(Pos42 – OFF). These spectra represent the surface brightness difference relative to the mean sky brightness in the transparent surroundings of the cloud, represented by the OFF positions 18, 20, 24, 25, 32, 34 and 36 (see table 1 of Paper I). The results refer to the corrected spectra, i.e. outside-the-atmosphere. In the following they will be referred to, for simplicity, without the superscript '0'. The mean values for Pos9 and Pos42 will be designated by $\Delta I(\lambda)$(Pos9/42 – OFF) and $\Delta I(\lambda)$(Pos9/42–Pos8).

2.1 The components of the cloud spectrum

The following components contribute to the surface brightness difference 'dark cloud minus surrounding sky'.

(A) We designate the isotropic EBL as seen by an observer outside the Galaxy $I_{\rm EBL}(\lambda)$. It is attenuated by the intervening dust along the line of sight (LOS) and there is additional light scattered from the all-sky isotropic EBL into the LOS; (a) towards the comparison (OFF) fields we see almost unattenuated LOS EBL; (b) towards the opaque cloud position, Pos8, we see almost completely attenuated LOS EBL plus a weak scattered EBL signal and (c) towards the translucent cloud positions, Pos9 and Pos42, we see moderately attenuated LOS EBL and a moderate scattered EBL signal. We designate the modified EBL signal $I'_{\rm EBL}(\lambda)$. It is discussed in Section 2.1.1.

(B) Light scattered by dust with all-sky ISL plus DGL as a source of illumination; (a) in the cloud and (b) in the comparison (OFF) fields; the spectrum is a modified copy of the ISL spectrum, i.e. a continuum with Fraunhofer lines and the 400 nm discontinuity.

(C) Light scattered by dust into the LOS with diffuse all-sky ionized-gas emission as a source of illumination; (a) towards the cloud positions and (b) towards the comparison (OFF) fields. The spectrum is dominated by the Balmer lines. The Galactic scattered light, including the components under (B) and (C), is designated $I_{\rm SCA}(\lambda)$ and will be discussed in Sections 2.1.2 and 2.1.3.

(D) Direct LOS diffuse emission by ionized gas; (a) towards the dark cloud positions Pos8, Pos9 and Pos42 and (b) towards the comparison (OFF) positions; the spectrum is an emission line spectrum dominated by strong Balmer lines plus a weak continuum. This component is designated $I_{\rm BAL}(\lambda)$ and will be discussed in Section 2.1.3.

Components (C) and (D) contribute substantially only to the wavelength slots where the stronger Balmer lines are present. The observed differential spectrum 'dark cloud (ON) minus surrounding sky (OFF)' can be represented as follows:

$$\Delta I_{\rm obs}(\lambda) = \Delta I'_{\rm EBL}(\lambda) + \Delta I_{\rm SCA}(\lambda) + \Delta I_{\rm BAL}(\lambda). \quad (1)$$

Notice that while $\Delta I_{\rm SCA}(\lambda) > 0$, the differences $\Delta I'_{\rm EBL}(\lambda)$ and $\Delta I_{\rm BAL}(\lambda)$ are negative since the EBL and the Balmer line contribution are larger at the OFF than at the ON positions.

2.1.1 The EBL signal

We consider first the idealized case with an EBL signal only and fully transparent OFF areas. Then, for an optical depth of $\tau_{\rm cl}$ through the cloud, we can write the difference $\Delta I'_{\rm EBL}(\lambda) = I'^{\rm on}_{\rm EBL}(\lambda) - I'^{\rm off}_{\rm EBL}(\lambda)$ in the form

$$\Delta I'_{\rm EBL}(\lambda) = I_{\rm EBL}(\lambda)[{\rm e}^{-\tau_{\rm cl}} + f_{\rm sca}(\tau_{\rm cl})] - I_{\rm EBL}(\lambda) =$$
$$= -I_{\rm EBL}(\lambda)[1 - {\rm e}^{-\tau_{\rm cl}} - f_{\rm sca}(\tau_{\rm cl})] =$$
$$= -h I_{\rm EBL}(\lambda), \quad (2)$$

Table 1. Calculated values of the effective blocking factor $h = 1 - e^{-\tau_{cl}} - f_{sca}(\tau_{cl})$ for a spherical cloud of different optical thicknesses (diameters) τ_{cl} and for isotropic incident radiation. The errors reflect the uncertainties of the scattering parameters a and g. Error estimates in parentheses are based on the values for $\tau_{cl} = 2$–16.

τ_{cl}	h
0.5	0.18 (±0.03)
1	0.32 (±0.06)
2	0.53 ± 0.10
4	0.75 ± 0.12
8	0.90 ± 0.09
16	0.95 ± 0.05
20	0.96 (±0.05)

where $f_{sca}(\tau_{cl})$ is the fraction of scattered EBL from the dark cloud and

$$h = 1 - e^{-\tau_{cl}} - f_{sca}(\tau_{cl}). \quad (3)$$

For a completely opaque cloud, $\tau_{cl} > > 1$, with non-scattering dust grains (i.e. albedo $a = 0$) $f_{sca}(\tau_{cl}) = 0$ and the correction factor is $h = 1$. For a finite optical depth and the presence of scattered light, its value is reduced below unity.

The calculation of h for the isotropic incident EBL and for a homogeneous spherical cloud has been presented in appendix 1 of Mattila (1976). Monte Carlo method was used to solve the radiative transfer problem for different values of τ_{cl} (=cloud diameter) and the scattering parameters of the grains, i.e. the albedo a and asymmetry parameter g. Using the values $a = 0.6 \pm 0.1$ and $g = 0.7$–0.8 (Mattila 1971), the values as given in Table 1 were found for h. They refer to the central part of the cloud disc, with an area of 1/10th of the disc area. Towards the opaque 'standard position', Pos8, with $A_V(\mathrm{Pos8}) \gtrsim 15$ mag (see section 3 and table 1 of Paper I), the directly transmitted EBL through the cloud is $<10^{-5}$, and the scattered EBL does not influence the ON − OFF difference $\Delta I_{EBL}(\lambda)$ by more than 5 per cent, i.e. the cloud's blocking efficiency is ∼95 per cent. Towards the two intermediate-opacity positions, Pos9 and Pos42, with $A_V \approx 1$ mag (see section 3 and table 1 of Paper I), the cloud blocks ∼30 per cent of the EBL. Towards the OFF positions with a mean extinction of $A_V(\mathrm{OFF}) \approx 0.15$ mag, the EBL blocking factor is ∼5 per cent, i.e. ∼95 per cent of the EBL signal is transmitted.

2.1.2 *Scattered Galactic light*

The spectrum of the scattered Galactic light from the cloud can be represented as the product of two factors:

$$I^{on}_{SCA}(\lambda) = \langle i_{GAL}(\lambda)\rangle G_{SCA}(\lambda), \quad (4)$$

where $\langle i_{GAL}(\lambda)\rangle$ stands for the normalized spectrum of the impinging Galactic light; it is normalized to = 1 at a reference wavelength λ_0, i.e.

$$\langle i_{GAL}(\lambda)\rangle = \langle I_{GAL}(\lambda)\rangle / \langle I_{GAL}(\lambda_0)\rangle \quad (5)$$

and $G_{SCA}(\lambda)$ accounts for the intensity of the scattered light as well as for the reddening (or bluening) caused by the wavelength-dependent scattering and extinction in the cloud. $G_{SCA}(\lambda)$ is assumed to be, over a limited wavelength range, a linear function of λ

$$G_{SCA}(\lambda) = G_{SCA}(\lambda_0)[1 + grad \times (\lambda - \lambda_0)]. \quad (6)$$

The intensity and spectrum of the Galactic light, as seen by a virtual observer at the cloud's location, are a function of the galactic coordinates, $I_{GAL}(\lambda) = I_{GAL}(\lambda, l, b)$. The radiation impinging at the cloud's surface from different directions l, b is multiply scattered by the dust grains in the cloud, and $\langle I_{GAL}(\lambda)\rangle$ is the weighted mean of $I_{GAL}(\lambda, l, b)$ over the sky, with the direction-dependent weighting function being determined by the scattering properties of dust and the cloud's optical thickness.

In Appendix A, a synthetic spectrum of the Galactic starlight has been calculated by using spectra of representative stars of different spectral classes. The mean ISL spectrum over sky as seen by a cloud at the $|z|$-distance of 85 pc, representative of L 1642, is shown in Fig. A1 in Appendix A. The normalized Galactic spectrum, $\langle i_{GAL}(\lambda)\rangle$, can be assumed to be closely the same for all positions in the cloud (i.e. Pos8, Pos9, Pos42) as well as for the OFF positions as far as the strengths of the Fraunhofer lines and 400 nm discontinuity are concerned. The absolute level and the wavelength dependence of $G_{SCA}(\lambda)$ will be different and this is accounted for by different values of $G_{SCA}(\lambda_0)$ and *grad*.

For the OFF positions, with $A_V \approx 0.15$ mag (see section 3 and table 1 of Paper I), the scattered Galactic light can be calculated using the optically thin approximation:

$$I^{off}_{SCA}(\lambda) = C_N \times \tau_{off}(\lambda) \times \langle i_{GAL}(\lambda)\rangle. \quad (7)$$

The absolute level is normalized using the factor C_N so that at 555 nm $I^{off}_{SCA}(\lambda) = 3.34 \times 10^{-9}$ erg cm^{-2} s^{-1} sr^{-1} Å^{-1} . This value has been determined using the intermediate band photometry at 555 nm combined with ISOPHOT[1] 200 μm absolute surface photometry (see appendix C of Paper I). The wavelength dependence of extinction has been adopted from Cardelli, Clayton & Mathis (1989). The albedo of the dust has been taken to be constant over the wavelength range considered in this paper; this is justified by the results of Laureijs, Mattila & Schnur (1987). Because $\tau_{off}(\lambda)$ increases towards shorter wavelengths, $I^{off}_{SCA}(\lambda)$ is bluer than the integrated Galactic light represented by $\langle i_{GAL}(\lambda)\rangle$.

2.1.3 *Direct line-of-sight emission by ionized gas*

There is an all-sky diffuse light component caused by the widely distributed ionized gas. The strongest features in the optical spectrum are the Balmer emission lines; in addition, a weak Balmer continuum emission and other emission lines are present, such as [O II] 372.8 nm, [O III] 500.7 nm, [N II] 654.8 and 658.3 nm, and [S II] 671.6 and 673.1 nm (Brandt & Draine 2012; Lehtinen & Mattila 2013). The Balmer lines are present as strong absorption lines in the ISL spectrum (see Fig. A1 of Appendix A). They could, in principle, serve as good measures of the dark cloud's scattered ISL if there were not the emission lines from the ionized gas. The corrections for H β and H γ are so large that these lines have to be excluded from the scattered light separation analysis. However, the Balmer emission lines at $\lambda < 400$ nm, H ϵ, H_8, H_9 and H_{10} are much weaker and cause only small corrections to the ISL spectrum; their contributions can be estimated from H β, H γ and H δ lines using the Balmer decrement valid for diffuse interstellar gas.

The relative Balmer line intensities have been adopted according to table 4.2 of Osterbrock & Ferland (2006) for Case B, low-density limit, $T_e = 10\,000$ K. The lines are broadened to fit the observed, instrumentally broadened line profiles. The continuum has been adopted according to Aller (1984), table 4.9, $T_e = 10\,000$ K.

[1] Infrared Space Observatory.

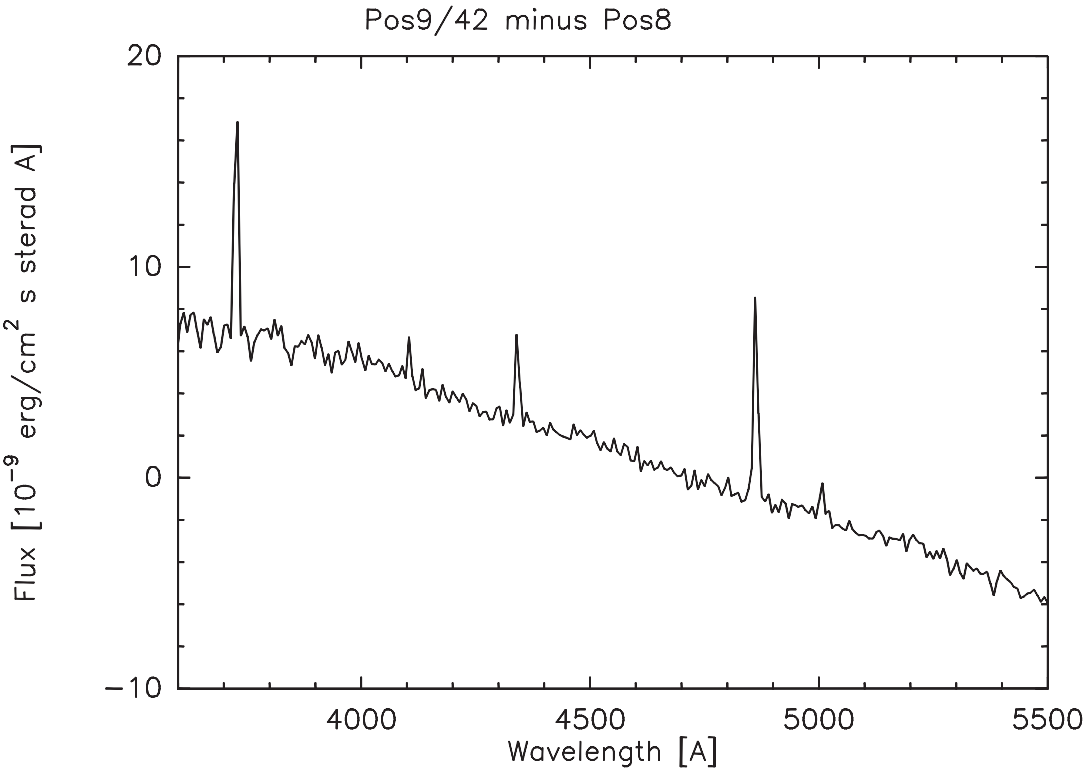

Figure 1. The differential spectrum $\Delta I(\lambda)$ (Pos9/42–Pos8). The emission lines in this spectrum are due to the gas located *behind* the cloud. Besides the Balmer lines H β, H γ and H δ also the [O II] line at 372.8 nm and [O III] line at 500.7 nm are seen. The line intensities are attenuated by extinction when transmitted through the dust layer of $A_V \sim 1$ mag at Pos9 and Pos42.

Table 2. Intensities of spectral lines in the differential spectrum $\Delta I(\lambda)$(Pos9/42–Pos8) (see Fig. 1). Unit for line areas is 10^{-9} erg cm^{-2} s^{-1} sr^{-1} and for peak intensities 10^{-9} erg cm^{-2} s^{-1} sr^{-1} Å^{-1}. The model fit is given for LOS optical depth of $\tau_1(\mathrm{H}\,\beta) = 0.90$ for Pos9/42. In the last line is given the derived H β intensity for the background emission.

Line	Observed line		Model	
	Area	Peak	τ_1	Area
H β	112.8 ± 2.8	9.8	0.90	112.8
H γ	46.1 ± 2.8	5.1	1.03	46.1
H δ	18.7 ± 3.2	2.4	1.11	23.4
[O II] 372.8 nm	135.0 ± 6.9	13.2		
[O III] 500.7 nm	20.7 ± 2.3	2.2		
Derived background H β intensity				227

When using the observed spectrum at Pos9/42 as proxy for the impinging Galactic light spectrum $\langle i_{\mathrm{GAL}}(\lambda)\rangle$ (see Section 2.2.3 below), the scattered light not only from the ISL and DGL but also from the all-sky Balmer line (and continuum) emission is included in it.

Emission by the gas layer *in front* of the cloud cancels out, on average, in the differential spectra $\Delta I(\lambda)$(Pos8–OFF) and $\Delta I(\lambda)$(Pos9/42–OFF). The intensity of the direct LOS Balmer line emission from the *background* gas, $I^{\mathrm{bg}}_{\mathrm{BAL}}(\lambda)$ can be estimated as follows: Because of the large extinction, $I^{\mathrm{bg}}_{\mathrm{BAL}}(\lambda)$ is negligible towards Pos8 and only its contribution at OFF and at positions 9 and 42 has to be considered. Because of the transmitted background light, the differential spectrum $\Delta I(\lambda)$(Pos9/42–Pos8) shows the Balmer lines in emission (see Fig. 1). In Table 2, the line areas and peak values, as obtained from this spectrum, are given for the H β, H γ, H δ, [O II] 372.8 nm and [O III] 500.7 nm lines. The peak values were derived from the line areas using the line width of 10.5 Å as determined by the spectral resolution. We designate the optical depth through the cloud at Pos9/42 $\tau_1(\lambda)$. Then, the background H β intensity, $I^{\mathrm{bg}}_{\mathrm{BAL}}(\mathrm{H}\beta)$, can be calculated from $\Delta I(\mathrm{H}\beta)(\mathrm{Pos9/42} - \mathrm{Pos8}) = I^{\mathrm{bg}}_{\mathrm{BAL}}(\mathrm{H}\,\beta)\mathrm{e}^{-\tau_1(\mathrm{H}\beta)}$.

The omission of the *scattered* H β line contribution is justified because the scattered light intensity at the wavelength of H β is closely the same for Pos8 and Pos9/42 and thus cancels out in their difference (see fig. 6 of Paper I).

We have adopted for the optical depth the value $\tau_1(\mathrm{H}\beta) = 0.90$, which correctly reproduces the observed line ratio H β/H γ. It is somewhat smaller than the unweighted mean value for Pos9 and 42, $\tau_1(\mathrm{H}\,\beta) = 1.1 \pm 0.1$, but close to $\tau_1(\mathrm{H}\,\beta) = 0.94 \pm 0.1$ for Pos42, which dominates by its higher weight in the spectrum ΔI(Pos9/42–Pos8). (For the extinction values towards Pos9 and Pos42 see section 3 and table 1 of Paper I.)

In the model fitting procedure, the intensities of the Balmer lines and Balmer continuum relative to H β intensity are kept fixed and the whole spectrum is scaled by one and the same factor. At $\lambda > 380$ nm the level of Balmer continuum correction is always $\lesssim 0.25\,10^{-9}$ erg cm^{-2} s^{-1} sr^{-1} Å^{-1} . Its uncertainty is $\lesssim 10$ per cent, which means that the correction introduces no significant uncertainty to the EBL determination.

2.2 Model fitting of the observed spectrum of the opaque position

2.2.1 Cloud geometry

The high-opacity position Pos8 towards the centre of the cloud is bracketed by the intermediate-opacity positions 9 and 42 on its

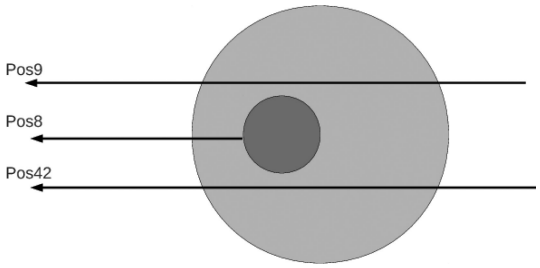

Figure 2. Schematic model of the cloud with opaque core embedded in a partly transparent envelope.

northern and southern side, separated from it by ∼10 and 7 arcmin, respectively. It is plausible that the dense core is located at about half way inside the lower opacity halo that has an extinction of $A_V \approx 1$ mag. Then, a layer with $A_V \approx 0.5$ mag would be located in front and a layer with $A_V \approx 0.5$ mag behind of it. Scattered light intensity from the layer in front of the core amounts to approximately half of the intensity at the positions 9 and 42. The model is schematically shown in Fig. 2. Variations on the model will be considered by placing the core at different fractional depths of $d = 0$, 0.3, 0.5 and 0.7 from the surface of the cloud.

2.2.2 *Model fit using the synthetic ISL spectrum*

Synthetic models of the ISL spectrum have been calculated as described in Appendix A. In order to test and validate such a spectrum, we have compared it with the observed mean spectrum for positions 9 and 42, $\Delta I(\lambda)$(Pos9/42–OFF) (see Appendix A, Fig. A1). At these positions, the obscuration of the EBL is small and the spectral shape is only weakly influenced by dust. The comparison shows that while the overall fit is good for $\lambda > 400$ nm, there is a substantial discrepancy with the 400 nm step size: the 'observed minus model' values deviate systematically upwards at $\lambda < 400$ nm, i.e. the ISL model predicts a larger step at 400 nm than the observed one. Such a behaviour cannot be explained by an EBL contribution. A residual EBL contribution would have an effect in the opposite direction.

Rather than trying to adjust the model parameters of the synthetic ISL spectrum, we will in the following use the observed Pos9/42 spectrum to derive a proxy for the impinging Galactic spectrum.

2.2.3 *Model fit using the observed scattered light spectrum*

We use the observed ON–OFF spectrum $\Delta I(\lambda)$(Pos9/42–OFF) to derive an expression for the 'total power' scattered light spectrum, $I_{\rm SCA}(\lambda)$(Pos9/42), which will be used as a proxy for the impinging all-sky Galactic light spectrum, $\langle i_{\rm GAL}(\lambda)\rangle$.

$$I_{\rm SCA}(\lambda)({\rm Pos9/42}) = \Delta I(\lambda)({\rm Pos9/42-OFF}) + I^{\rm off}_{\rm SCA}(\lambda) + \\ + h_1 I_{\rm EBL}(\lambda) + [1-\exp(-\tau_1(\lambda))] I^{\rm bg}_{\rm BAL}(\lambda). \quad (8)$$

The term for the scattered Galactic light at the OFF positions, $I^{\rm off}_{\rm SCA}(\lambda)$, will be estimated below. The moderate contribution by the EBL signal is corrected for by the term $h_1 I_{\rm EBL}(\lambda)$, where $h_1 \approx 0.32$ corresponding to $\tau_1 \approx 1$ (see Table 1). This correction term will be included into the final component separation procedure to be applied to the opaque position, Pos8, spectrum.

The direct LOS gas emission from the layer behind the cloud introduces two terms: (1) the transmitted light at Pos9/42, $\exp(-\tau_1) I^{\rm bg}_{\rm BAL}(\lambda)$(Pos9/42) and (2) the emission towards the OFF positions, $I^{\rm bg}_{\rm BAL}(\lambda)$(OFF). While the former term is known from the analysis of the spectrum $\Delta I(\lambda)$(Pos9/42–Pos8) (see Section 2.1.3 and Fig. 1), the latter term is not. In equation (8), we have assumed that $I^{\rm bg}_{\rm BAL}(\lambda)$ is equal for Pos9/42 and the OFF positions. Above, we have also assumed that the foreground Balmer emission is the same towards the cloud and the OFF positions, $I^{\rm fg}_{\rm BAL}(\lambda)$(Pos8) = $I^{\rm fg}_{\rm BAL}(\lambda)$(Pos9/42)= $I^{\rm fg}_{\rm BAL}(\lambda)$(OFF), and has thus cancelled out in the differential spectra. While fitting the spectrum $\Delta I(\lambda)$(Pos8–OFF), these approximations can be accounted for by adjusting the scaling of the Balmer line spectrum; it will be slightly different from the value found for Pos9/42, $I^{\rm bg}_{\rm BAL}(H\beta) = 26 \times 10^{-9}$ erg cm^{-2} s^{-1} sr^{-1} Å^{-1} . We notice that the terms $I^{\rm bg}_{\rm BAL}$ and $I^{\rm fg}_{\rm BAL}$ are important only for the wavelengths of Balmer lines.

For the OFF positions, with $A_V \approx 0.15$ mag, the scattered Galactic light can be represented using the optically thin approximation and the spectrum for positions 9 and 42, modified by a correction for the optical depth effect, $[1 - \exp(-\tau_1(\lambda))]^{-1}$:

$$I^{\rm off}_{\rm SCA}(\lambda) = C_{\rm N} \times \tau_{\rm off}(\lambda) \frac{I_{\rm SCA}(\lambda)({\rm Pos9/42})}{1-\exp(-\tau_1(\lambda))}. \quad (9)$$

Concerning the normalization factor $C_{\rm N}$ and the wavelength dependence of the optical depth, $\tau(\lambda)$, we refer to equation (7) above. Because $I^{\rm off}_{\rm SCA}(\lambda)$ and $I_{\rm SCA}(\lambda)$(Pos9/42) depend on each other according to equations (8) and (9), their values have to be determined iteratively. In practice, two iterations were found to be enough.

The observed spectrum $\Delta I(\lambda)$(Pos8–OFF) to be fitted in accordance with equations (1), (2) and (6) is the mean of the 'Master A&B Mean' and 'Secondary Mean' spectra (see section 8 and fig. 6 of Paper I). The spectrum is re-binned with 5-pixel boxcar function resulting in 0.7 nm bins, closely corresponding to the physical resolution.

For the fitting procedure, we used the IDL[2] programme `MPFITFUN`.[3] The function `MYFUNCT` used for the fitting of $\Delta I(\lambda)$(Pos8–OFF) is formulated as follows:

$$\texttt{MYFUNCT} = [p_0 + p_1(\lambda - \lambda_0)] I_{\rm SCA}(\lambda)({\rm Pos9/42}) - I^{\rm off}_{\rm SCA}(\lambda) \\ - h_0 I_{\rm EBL}(\lambda) - p_2 I_{\rm BAL}(\lambda). \quad (10)$$

The parameters p_0 and p_1 correspond to $G_{\rm SCA}(\lambda_0)$ and *grad* in equation (6); for λ_0 we use 400.0 nm. For $I_{\rm SCA}(\lambda)$(Pos9/42) and $I^{\rm off}_{\rm SCA}(\lambda)$, we use the spectra derived according to equations (8) and (9) from the spectrum $\Delta I(\lambda)$(Pos9/42–OFF). The EBL intensity, $I_{\rm EBL}(\lambda)$, is assumed to be constant over each of the limited wavelength intervals used for the fitting procedure. For the parameter h_0 corresponding to $\tau \gtrsim 15$ for Pos8, we adopt according to Table 1 the value $h_0 = 0.95$. The direct LOS Balmer emission will be scaled using the parameter p_2.

Equation (10) corresponds to the geometric model where the opaque core is located on the near side of the cloud envelope, i.e. $d = 0$. As discussed in Section 2.2.1 above, in a more likely geometric configuration the core is at an intermediate depth, say $d \sim 0.5$, within the cloud. We have run alternative model fits with this geometry in mind. Model-wise, we can peel off the foreground dust layer by modifying the observed spectrum for Pos8. In the case

[2] http://www.exelisvis.com/ProductsServices/IDL.aspx
[3] www.physics.wisc.edu/graigm/idl/fitting.html

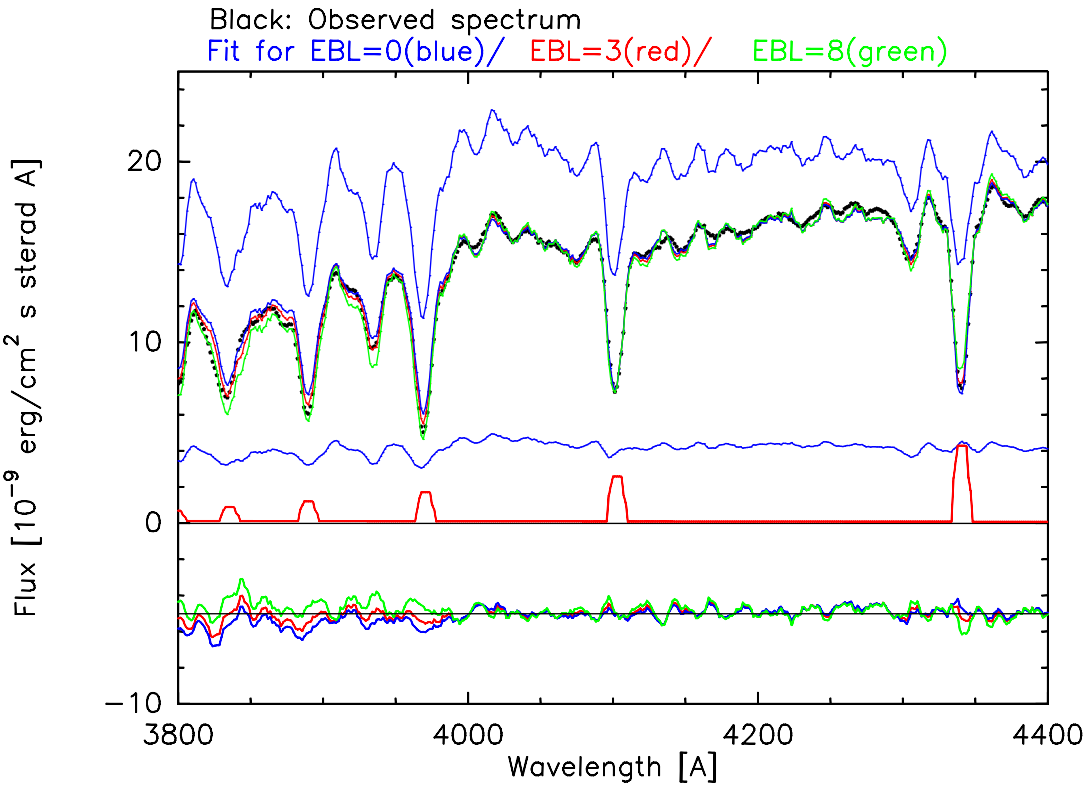

Figure 3. Demonstration of the use of the 400 nm discontinuity for the determination of the EBL. The spectrum $\Delta I(\lambda)$(Pos8–OFF) of the opaque central position 8 (black dots) is fitted with the Pos9/42 spectrum (topmost blue curve). Different values have been assumed for the EBL to demonstrate how they influence the goodness of the fit. The lower blue line is the mean scattered light OFF spectrum according to equation (9) and the red line the direct LOS ionized gas emission line OFF spectrum. The model fits are shown superimposed on the observed Pos 8 spectrum for three values, $I_{\rm EBL} = 0$ (blue), 3 (red) and 8 10^{-9} erg cm^{-2} s^{-1} sr^{-1} Å^{-1} (green). The residuals *observation minus fit* are shown at the bottom with the same colour coding. See the text for details.

that the core is located at a depth d within the cloud, the observed spectrum for Pos8 is replaced by

$$\Delta I(\lambda)(\mathrm{Pos8} - \mathrm{OFF}) - d \times \Delta I(\lambda)(\mathrm{Pos9/42} - \mathrm{OFF})$$

and `MYFUNCT` is modified as follows:

`MYFUNCT` =

$$= [p_0 + p_1(\lambda - \lambda_0))]I_{\rm SCA}(\lambda)(\mathrm{Pos9/42}) - (1-d)I^{\rm off}_{\rm SCA}(\lambda)$$
$$- (h_0 - h_1 d)I_{\rm EBL}(\lambda) - (1 - d + de^{-\tau_1(\lambda)})p_2 I_{\rm BAL}(\lambda). \qquad (11)$$

In the `MPFITFUN` fitting run, p_0, p_1 and $I_{\rm EBL}$ are free parameters that are simultaneously determined by least squares fitting. The scaling factor p_2 for the Balmer emission is determined in a separate fitting procedure applied to the Balmer lines only, and its value is kept fixed in the main fitting procedure. The quality of the fit is judged by the χ^2 value that results from the fit.

3 RESULTS FROM `MPFITFUN` FITTING

Promising spectral features for the separation of the scattered light are the 400 nm discontinuity, the strong Fraunhofer lines H and K of Ca II at 397 and 393 nm, and the *G* band at 430 nm. To a lesser extent the Mg I+Mg *H* band at 517 nm and the Fe line at 527 nm can be useful for setting at least an upper limit to $I_{\rm EBL}$. Balmer lines H β, H γ and H δ would appear as good candidates because they are strong in the ISL spectrum (see Fig. A1 of Appendix A). However, because they are present in the direct LOS ionized gas emission as well, they do not enable an estimation of the scattered light. Nevertheless, one can use them to estimate the contamination effect which H ϵ has on the Ca II H line, and H_8, H_9 and H_{10} on the overall mean intensity level at 380–390 nm.

3.1 Results from different wavelength slots

We first demonstrate qualitatively that the spectroscopic separation method is capable of reaching the required sensitivity level of $\lesssim$ 1 10^{-9} erg cm^{-2} s^{-1} sr^{-1} Å^{-1} . In Fig. 3, we demonstrate the use of the 400 nm discontinuity to the determination of the EBL. The 380–440 nm spectrum of the opaque central position 8 (black dots) is shown together with the Pos9/42 spectrum according to equation (8). The lower blue curve at $\sim 4 \times 10^{-9}$ erg cm^{-2} s^{-1} sr^{-1} Å^{-1} is the scattered light spectrum for the OFF positions (equation 9). The red line shows the correction for the direct LOS Balmer emission lines.

Model fits are shown superimposed on the observed spectrum for $I_{\rm EBL} = 0$ (blue), 3×10^{-9} erg cm^{-2} s^{-1} sr^{-1} Å^{-1} (red) and 8×10^{-9} erg cm^{-2} s^{-1} sr^{-1} Å^{-1} (green), respectively. The residuals, *observation minus fit*, are shown as the bottom-most three curves. Their deviations from zero level at $\lambda < 400$ nm reflect the influence of the 400 nm step size. For $I_{\rm EBL} = 0$ the step size of the model fit is smaller while for $I_{\rm EBL} = 8$ 10^{-9} erg cm^{-2} s^{-1} sr^{-1} Å^{-1} it is larger than the observed one. For an intermediate value of $I_{\rm EBL} =$ 3 10^{-9} erg cm^{-2} s^{-1} sr^{-1} Å^{-1} a good agreement is reached.

In Fig. 4 we demonstrate the use of the H and K lines to the determination of the EBL. The 390–400 nm spectrum of the opaque position 8 (black dots) is again fitted with the Pos9/42 spectrum (blue

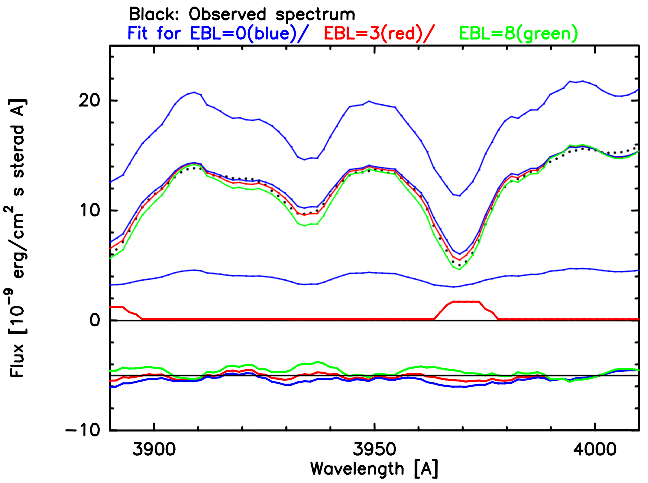

Figure 4. Demonstration of the use of the Ca H and K lines for the determination of the EBL as in Fig. 3. The 390–400 nm spectrum of the opaque position 8 (black dots) is fitted with the Pos9/42 spectrum (topmost blue line) for three assumed values of the EBL. The lower blue line is the scattered light spectrum and the red line the ionized hydrogen emission line spectrum for the OFF positions. The fits are shown superimposed on the observed spectrum for position 8 for three values of the EBL intensity, $I_{\rm EBL} = 0$ (blue), 3 (red) and 8×10^{-9} erg cm^{-2} s^{-1} sr^{-1} Å^{-1} (green). The residuals *observation minus fit* are shown as the bottom-most three curves with the same colour coding and with zero level shifted by -5×10^{-9} erg cm^{-2} s^{-1} sr^{-1} Å^{-1}. See the text for details.

line) for three values of the EBL. The fitted spectra are deciphered in the same way as in Fig. 3. Comparison of the fitted line depths with the observed ones indicates that for $I_{\rm EBL} = 0$ the model predicts too shallow lines while for $I_{\rm EBL} = 8 \times 10^{-9}$ erg cm^{-2} s^{-1} sr^{-1} Å^{-1} they are deeper than the observed ones. Again, the intermediate value of $I_{\rm EBL} = 3\ 10^{-9}$ erg cm^{-2} s^{-1} sr^{-1} Å^{-1} gives the best fit.

In Table 3 we give $I_{\rm EBL}$ values and their statistical errors, $\sigma_{\rm fit}$, obtained from MPFITFUN fitting for seven cases. The wavelength slots used are given in the second column. The third column gives the relevant spectral features that are facilitating the separation of the scattered light from the EBL. The EBL values and their 1σ statistical errors or 2σ upper limits are given in the fifth and sixth column. Systematic errors follow in column 7.

The most sensitive probe is provided by the case where both the H and K lines and the 400 nm discontinuity are included in the fit. The first result is for the 50 nm wide range, $\lambda = 381$–432.5 nm, which includes also the Balmer lines H δ to H$_9$. The Balmer line scaling factor is included as a free parameter in the fitting. Its value is thereby well determined mainly by the H δ line that is not blended with other spectral features.

Although all the Balmer lines at $\lambda < 400$ nm are substantially weaker than H δ, there may still be a residual effect, especially because of the H ϵ line at 397 nm that is blended with the Ca II H line. As the second case we have, therefore, made a fit to the same wavelength range, $\lambda = 381$–432.5 nm, but excluding all Balmer lines and thereby also the H line of Ca II.

In the third case even the K line has been excluded and the result is thus based mainly on the 400 nm jump only. In the fourth case we use a narrow window, including the H and K lines only, while in the fifth case only the K line is included.

The error estimates, $\sigma_{\rm fit}$, as given by MPFITFUN, are seen to increase while the wavelength window is narrowed down. The first four cases provide significant $I_{\rm EBL}$ values ($\gtrsim 2\sigma$ detections) in agreement with each other. In the fifth case the error is too large to allow an EBL detection.

A fit to the *G* band alone (Case 6) can be used to set an upper limit of $I_{\rm EBL} \leq 5.0 \times 10^{-9}$ erg cm^{-2} s^{-1} sr^{-1} Å^{-1} (2σ). The region 510–530 nm includes two relatively strong Fraunhofer lines, Mg H+Mg I at 517 and Fe at 527 nm. The fitting allows an upper limit to be set to the EBL at 520 nm, $I_{\rm EBL} \leq 4.5\ 10^{-9}$ erg cm^{-2} s^{-1} sr^{-1} Å^{-1} (2σ) (Case 7).

3.2 Errors caused by zero-level uncertainties of the observed spectra

The observational errors of the spectra $\Delta I(\lambda)$(Pos8–OFF), $\Delta I(\lambda)$(Pos9/42–Pos8) and $\Delta I(\lambda)$(Pos9/42–OFF) can be separated into three categories: (1) the pixel-to-pixel statistical errors; (2) the error of the zero level, which for $\Delta I(\lambda)$(Pos8–OFF) is partly statistical and partly caused by the uncertainties of the differential ADL and ZL corrections; and (3) the calibration errors.

The effect of the pixel-to-pixel statistical errors is taken into account by the MPFITFUN fitting procedure. The effect of calibration errors is straight forward and will be added to the errors resulting from the modelling (see Section 3.4 below).

It has been found in section 8.1 of Paper I that the zero-point error of $\Delta I(\lambda)$(Pos8–OFF) is $\pm 0.5 \times 10^{-9}$ erg cm^{-2} s^{-1} sr^{-1} Å^{-1} . Because the spectrum $\Delta I(\lambda)$(Pos9/42–OFF) was calculated as the sum of $\Delta I(\lambda)$(Pos9/42–Pos8) and $\Delta I(\lambda)$(Pos8–OFF) it is subject to the same zero-level error as $\Delta I(\lambda)$(Pos8–OFF). In addition, it has the zero-point error inherent in the spectrum $\Delta I(\lambda)$(Pos9/42–Pos8). This error was found to be $\sim\pm$ 0.47 10^{-9} erg cm^{-2} s^{-1} sr^{-1} Å^{-1} at $\lambda \approx 400$ nm; and $\sim\pm$ 0.63 10^{-9} erg cm^{-2} s^{-1} sr^{-1} Å^{-1} at $\lambda \approx$ 520 nm (see section 8.1 and table 3 of Paper I). For the spectrum $\Delta I(\lambda)$(Pos9/42–Pos8), because the positions 8, 9 and 42 have small angular separations, the ADL and ZL corrections are unimportant and the error is purely statistical.

In order to investigate the effects of these zero-point errors we have run the MPFITFUN fitting procedure

(1) for the three cases where a zero-point correction of -0.5, 0.0, and $+0.5 \times 10^{-9}$ erg cm^{-2} s^{-1} sr^{-1} Å^{-1} was applied to both $I(\lambda)$(Pos8–OFF) and $I(\lambda)$(Pos9/42–OFF); and (2) for each of these three cases we have applied, in addition, a correction to the spectrum $I(\lambda)$(Pos9/42–OFF) of -0.47, 0.0, and $+0.47 \times 10^{-9}$ erg cm^{-2} s^{-1} sr^{-1} Å^{-1} for $\lambda = 381$–433 nm, or -0.63, 0.0, and $+0.63 \times 10^{-9}$ erg cm^{-2} s^{-1} sr^{-1} Å^{-1} for $\lambda \approx$ 520 nm.

The former zero-point corrections change the EBL value by $\pm 0.13 \times 10^{-9}$ erg cm^{-2} s^{-1} sr^{-1} Å^{-1} . Because this error is partly caused by uncertainties in the differential ADL and ZL corrections we conservatively assign it as a systematic error. It is given as the first item ($\sigma_{\rm zero}$) in column (7). The latter zero-level uncertainty causes a statistical error. It amounts to $\sigma_{\rm zero} = \pm 0.70$ and $\pm 1.20 \times 10^{-9}$ erg cm^{-2} s^{-1} sr^{-1} Å^{-1} at $\lambda = 381$–433 and 520 nm, respectively. It is given as the second item in the sixth column of Table 3.

3.3 Errors caused by modelling uncertainties

In addition to the observationally based errors there are errors caused by uncertainties in the modelling. These are the uncertainties of $I^{\rm off}_{\rm SCA}(\lambda)$, the scattered light intensity at the OFF positions; the scaling of $I_{\rm BAL}(\lambda)$, the direct LOS Balmer line intensity; the uncertainties of the effective blocking factors h_0 and h_1; and the influence of the wavelength dependence of $I_{\rm EBL}$.

Table 3. EBL values from MPFITFUN fitting utilizing different spectral features of the scattered ISL. Statistical errors are given as resulting from the pixel-to-pixel noise of the spectra (see Section 3.1), the zero-level uncertainty of the $\Delta I(\lambda)$(Pos9/42–Pos8) spectrum (Section 3.2), and the Balmer line correction (Section 3.3). Their quadratic sum is $\sigma_{\rm tot}$. The upper limits given for cases 6 and 7 include also the systematic error caused by the zero-level uncertainty of the Pos8–OFF spectrum (Section 3.2).

No.	Wavelength range (nm)	Spectral features used for fit	Remarks	$I_{\rm EBL}$[a]	Statistical errors[a] $\sigma_{\rm fit}$, $\sigma_{\rm zero}$, $\sigma_{\rm Bal}$, $\sigma_{\rm tot}$, $\sigma_{\rm cal}$	Systematic err[a] $\sigma_{\rm zero}$, $\sigma_{\rm model}$
(1)	(2)	(3)	(4)	(5)	(6)	(7)
1	381–432.5	400 nm jump, G, Ca II H+K	H δ, H ϵ, H ζ, H$_9$ included	3.20	0.81 0.70 0.3 1.11 9%	$0.13\,^{+18\%}_{-13\%}$
2	381–382.5, 385–387.5, 390–396, 398–408, 412–432.5	400 nm jump, G, Ca II K	Balmer lines and Ca II H excluded	2.54	0.94 0.70 – 1.17 9%	$0.13\,^{+18\%}_{-13\%}$
3	381–382.5, 385–387.5, 390–392.5, 398–408, 412–432.5	400 nm jump, *G* band	Balmer lines and Ca II H+K excluded	2.54	1.16 0.70 – 1.35 9%	$0.13\,^{+18\%}_{-13\%}$
4	390–399	Ca II H+K	H ϵ included	3.58	1.42 0.70 0.5 1.66 9%	$0.13\,^{+18\%}_{-13\%}$
5	390–396	Ca II K	Ca II K only	1.76	1.86 0.70 – 1.99 9%	$0.13\,^{+18\%}_{-13\%}$
6	425–432.5, 436–445	*G* band	*G* band only	$\leq$5.0 (2σ) 0.84	1.91 0.70 – 2.03 9%	$0.13\,^{+18\%}_{-13\%}$
7	510–519, 522–530	Mg517, Fe527	520 nm airglow line excluded	$\leq$4.5 (2σ) −1.80	2.40 1.20 – 2.70 9%	$0.84\,^{+18\%}_{-13\%}$

[a] $I_{\rm EBL}$ and errors are units of 10^{-9} erg cm^{-2} s^{-1} sr^{-1} Å^{-1} except for $\sigma_{\rm cal}$ and $\sigma_{\rm model}$, which are in per cent of the $I_{\rm EBL}$ value.

3.3.1 *OFF-position scattered light intensity*

We have varied $I^{\rm off}_{\rm SCA}(\lambda)$, given by equation (9), by scaling it up and down by 30 per cent. This corresponds to the extinction uncertainty of $\pm$0.05 mag at the OFF positions. This scaling had no effect on the derived EBL value. This, at first sight, surprising result can be understood because the spectral features in the OFF spectrum are the same as in the Pos9/42 spectrum used for the fitting. Thus, the scaling of the OFF spectrum does not change the strengths (equivalent widths) of the spectral features in the Pos9/42 spectrum. The spectral separation method is sensitive to the different absorption feature strengths of the Pos8 and Pos9/42 spectra, and not to their overall scaling difference.

3.3.2 *Balmer line intensities*

The Balmer line scaling factor p_2 [see equations (10) and (11)] was determined using the H δ line. While H δ itself was included only in the first EBL fit as given in Table 3 it was used to give the scaling for H ϵ included in the EBL determination for the wavelength slot 390–399 nm (fourth case in Table 3). The statistical uncertainty of p_2, as determined from the fitting of H δ line was found to be $\pm$10 per cent. This causes to the EBL estimate an error of $\pm 0.5 \times 10^{-9}$ erg cm^{-2} s^{-1} sr^{-1} Å^{-1} as given as the fourth value in column (6) of Table 3.

3.3.3 *Case of the embedded dense core*

Fig. 5 illustrates the case where an envelope layer has been 'peeled off' in front of the opaque core (see model in Section 2.2.1 and Fig. 2). The core has been assumed to be half way between the front and back surface of the envelope, i.e. $d = 0.5$. The spectrum to be fitted in this case is

$$\Delta I(\lambda)(\text{Pos8} - \text{OFF}) - 0.5 \times \Delta I(\lambda)(\text{Pos9/42} - \text{OFF}),$$

and equation (11) with $d = 0.5$ will be used in MPFITFUN instead of equation (10). A fit to the spectrum in the interval 380–432.5 nm with $I_{\rm EBL} = 3 \times 10^{-9}$ erg cm^{-2} s^{-1} sr^{-1} Å^{-1} is shown as red line superimposed on the 'peeled off' spectrum shown as black dots.

Somewhat surprisingly, the result for $I_{\rm EBL}$ is the same as for the case $d = 0$. Also for the other values, $d = 0.3$ and 0.7, the same is true. This result can be understood because the spectrum of the surface layer, removed in front of the core, has the same Pos9/42 spectrum that is used in the fitting procedure. This outcome demonstrates that our fitting results for the EBL do not depend on the geometrical model, i.e. on the assumed location of the opaque core within the cloud envelope.

3.3.4 *Effect of the cloud's blocking factor*

We have varied the effective blocking factors from their adopted values of $h_0 = 0.95$ and $h_1 = 0.32$ by $\pm$0.05 and $\pm$0.06, i.e. by their uncertainties as listed in Table 1 for $\tau_{\rm cl} \geq 16$ and $\tau_{\rm cl} = 1$. The maximum deviations of the $I_{\rm EBL}$ value of +18 per cent and −13 per cent resulted for the parameter pairs $h_0 = 1.0$, $h_1 = 0.26$ and $h_0 = 0.90$, $h_1 = 0.38$, respectively.

3.3.5 *Effect of the EBL spectral shape*

We have finally tested the effect of a non-constant $I_{\rm EBL}(\lambda)$ spectrum. We assume a linear dependence with wavelength of the form $I_{\rm EBL}(\lambda) = I_{\rm EBL}(400\,{\rm nm})[1 + C(\lambda - 400\,{\rm nm})]$ and with a large gradient, $C = +0.5$ and -0.5 per 100 nm, respectively. For these two extreme gradients the resulting $I_{\rm EBL}$ values for the second case in Table 3 differed by $\leq \pm 3$ per cent. The effect on the other $I_{\rm EBL}(\lambda)$ values in Table 3, covering the same or smaller wavelength range, is equal or smaller than this.

3.4 The EBL results at 400 and 520 nm

In Table 3 the first two EBL estimates are based on the same wavelength slot, λ = 381–432.5 nm, one with and the other without the Balmer lines. The two $I_{\rm EBL}$ values are not independent. The good

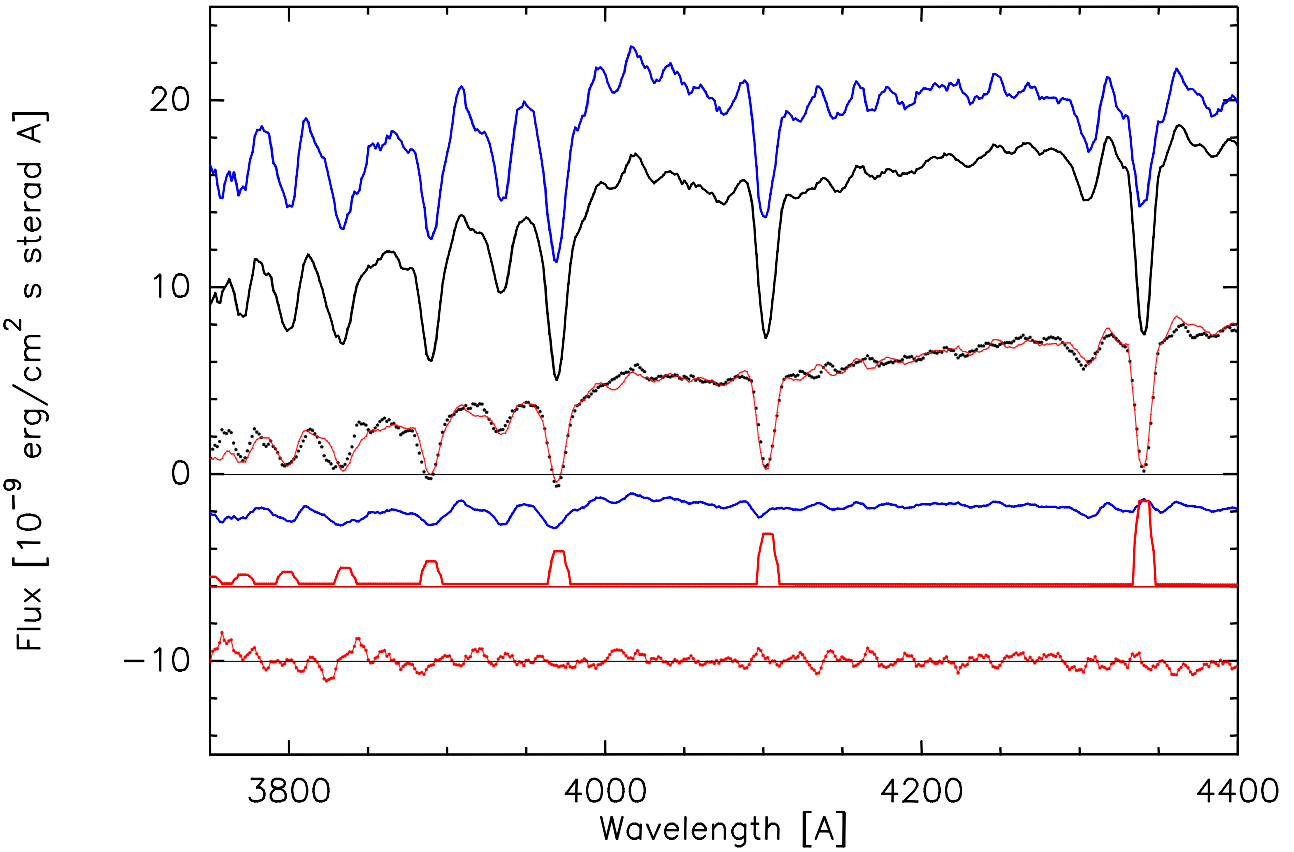

Figure 5. Demonstration that the derived EBL value is not sensitive to the assumed location of the opaque core within the cloud envelope. The observed spectrum for position 8 is shown as upper black line and the 'peeled off' spectrum after subtraction of 0.5 × the Pos9/42 spectrum as black dots. Pos9/42 spectrum is the upper blue line. The lower blue line is the scattered light and the red line the gas emission spectrum for the OFF positions (both shifted by –6 units). The modelled spectrum for $I_{\rm EBL}$ = 3 10^{-9} erg cm^{-2} s^{-1} sr^{-1} Å^{-1} is shown as red line superimposed on the 'peeled off' dense core spectrum. The residuals *observation minus fit* are shown at bottom (shifted by –10 units). See the text for details.

agreement between them demonstrates, however, that our correction for the Balmer line contamination is reasonably good. The two strongest spectral features of the scattered Galactic light spectrum in this wavelength range are the 400 nm jump and the H and K lines of Ca II. The third case in Table 3 excludes, besides all Balmer lines and H, also the K line. The result is thus based essentially on the 400 nm jump only.

In the fourth case we have limited the wavelength range to a narrow window covering the H and K lines only. The result is thus independent of the 400 nm discontinuity. Using a window that includes the K line only (Case 5) the fitting error becomes too large to allow a useful $I_{\rm EBL}$ estimate.

All $I_{\rm EBL}$ values as derived for cases 1–4 agree within a fraction of their $1\sigma_{\rm tot}$ statistical errors. The first two values, based on the largest number of spectral elements, have the smallest statistical errors. Their unweighted mean value can thus be considered a good choice in this wavelength range: $I_{\rm EBL}$ = 2.87 ± 1.1 10^{-9} erg cm^{-2} s^{-1} sr^{-1} Å^{-1}. Because the two values are not independent the error of their mean is not reduced below the individual errors. Another estimate with comparable precision is the mean of the third and fourth $I_{\rm EBL}$ values that are independent. Their weighted mean and its standard error is $I_{\rm EBL}$ = 2.95 ± 1.0 × 10^{-9} erg cm^{-2} s^{-1} sr^{-1} Å^{-1}. As weights we have used the $\sigma_{\rm tot}^{-2}$ values.

The two mean values (1 and 2) and (3 and 4) are, somewhat fortuitously, almost equal and have almost the same standard error. We adopt their mean value as our final choice in the wavelength region λ = 380–432.5 nm: $I_{\rm EBL} = 2.9 \pm 1.0 \times 10^{-9}$ erg cm^{-2} s^{-1} sr^{-1} Å^{-1} .

In Section 3.2 we saw that an error of ± 0.13 × 10^{-9} erg cm^{-2} s^{-1} sr^{-1} Å^{-1} was caused by the zero-level uncertainty of ΔI(λ)(Pos8–OFF). If we conservatively assume that most of it is systematic it has to be added linearly to the statistical error resulting in: $I_{\rm EBL}$ = 2.9 ± 1.1 10^{-9} erg cm^{-2} s^{-1} sr^{-1} Å^{-1} .

The multiplicative error consists of the spectrophotometric calibration error of ±9 per cent (see section 8.2 of Paper I), the uncertainty caused by the blocking factor of +18 per cent/−13 per cent, and an error of maximally ±3 per cent caused by possible wavelength dependence of $I_{\rm EBL}$(λ). Quadratic addition results in the total multiplicative error of +20 per cent/−16 per cent. It increases or decreases the $I_{\rm EBL}$ value and its statistical error limits in the same way and, therefore, does not influence the statistical significance level (2.6σ) of our EBL detection.

Our result for the wavelength range λ = 381–432.5 nm can thus be written in the form:

$I_{\rm EBL}$ = 2.9 ± 1.1 10^{-9} erg cm^{-2} s^{-1} sr^{-1} Å^{-1} +20 per cent/−16 per cent, or 11.6 ± 4.4 nW m^{-2} sr^{-1} +20 per cent/−16 per cent.

The two upper limits for $I_{\rm EBL}$, at λ ∼ 430 nm and at λ ∼ 520 nm, given in Table 3 as cases 6 and 7, are based on their statistical error estimates, $\sigma_{\rm tot}$, complemented by the partly systematic error caused by the zero-level uncertainty of ΔI(λ)(Pos8–OFF). In Case 6 (λ ∼ 430 nm) the error caused by the zero uncertainty is again ±0.13 × 10^{-9} erg cm^{-2} s^{-1} sr^{-1} Å^{-1} . In Case 7 (λ ∼ 520 nm) it is

Table 4. Contribution of resolved galaxies in the 2 arcsec slit at the OFF positions. The columns give position name (1) and indicate whether chip 1, 2 or both were used for the spectrum (2). Then follows the date of the spectrum (3). In columns (4)–(6) the date, integration time (in seconds) and filter are given for the images. Columns (7) and (8) give the magnitude range of galaxies and their contribution to the EBL in units of 10^{-9} erg cm^{-2} s^{-1} sr^{-1} Å^{-1} .

Position (1)	Chip (2)	Date Spectrum (3)	Date Deep image (4)	Int. time (5)	Filter (6)	Magnitude range (7)	EBL contribution (8)
Master spectra							
POS18	1	2003-10-20	2011-10-02	600	B_HIGH	24.0–26.8	0.50
POS20	1 and 2	2010-12-14	2010-12-14	600	B_HIGH	22.4–26.1	0.57
POS24	1	2003-10-20	2009-01-29	600	B_HIGH	23.3–26.3	0.40
POS24	1 and 2	2004-09-18	2009-01-29	600	B_HIGH	23.2–26.3	0.58
Mean							0.51
Secondary spectra							
POS18	1 and 2	2011-10-02	2011-10-02	600	B_HIGH	24.0–26.8	0.42
POS24	1 and 2	2004-02-18	2009-01-29	600	B_HIGH	23.7–26.2	0.44
POS25	1 and 2	2004-01-25	2004-01-25	90	B_BESS	22.3–24.3	0.44
POS32	1 and 2	2004-01-25	2004-01-25	90	B_BESS	21.9–24.4	0.74
POS34a	2	2004-09-16	2009-01-30	600	B_HIGH	22.7–26.5	1.11
POS34b	1 and 2	2004-01-24	2009-01-30	600	B_HIGH	23.6–25.6	0.29
POS36	1 and 2	2003-11-24	2011-10-27	600	B_HIGH	23.0–26.0	0.36
Mean							0.54

$\pm 0.84\ 10^{-9}$ erg cm^{-2} s^{-1} sr^{-1} Å^{-1} . The multiplicative error is the same as above.

We thus end up with the following final 2σ upper limits:

$I_{\rm EBL} \leq 5.0 \times 10^{-9}$ erg cm^{-2} s^{-1} sr^{-1} Å^{-1} +20 per cent/−16 per cent, or

$\leq$20.0 nW m^{-2}sr^{-1} +20 per cent/−16 per cent at 430 nm, and

$I_{\rm EBL} \leq 4.5 \times 10^{-9}$ erg cm^{-2} s^{-1} sr^{-1} Å^{-1} +20 per cent/−16 per cent, or

$\leq$23.4 nW m^{-2} sr^{-1} +20 per cent/−16 per cent at 520 nm.

4 DISCUSSION

4.1 Contribution by resolved galaxies

Part of our measured EBL signal is caused by resolved galaxies in the slit area. The slit positions were chosen to avoid stars and galaxies visible on the DSS2 blue plates. This corresponds to $B \approx$ 22 mag. In order to measure the contribution of galaxies fainter than this limit we have secured for each one of our fields as listed in table 2 of Paper I a direct $\sim 6.8 \times 6.8$ arcmin B-band image using VLT with FORS1 or FORS2 (see Table 4). For positions 18, 20, 24, 34 and 36, with integration time of $t_{\rm int} = 600$ s, the limiting magnitude was ∼26.5 mag, and for Pos25 and Pos32 with $t_{\rm int} = 90$ s it was ∼25.5 mag. Accurate positioning of the slit relative to the direct image was secured by taking immediately before each spectrum exposure a 10 s acquisition image after which the telescope pointing was kept fixed.

The images were bias-subtracted and flat-fielded and zero-point and extinction corrections were applied using the ESO Quality Control nightly zero-points and extinction coefficients for FORS1[4] and FORS2.[5] Kron magnitudes of all objects were determined using the SExtractor software (Bertin & Arnouts 1996) from within the Starlink GAIA v4.4.6 package.

[4] http://www.eso.org/observing/dfo/quality/FORS1/qc/zeropoints/zeropoints.html

[5] http://www.eso.org/observing/dfo/quality/FORS2/qc/zeropoints/zeropoints.html

The objects in the slit areas were visually inspected and most appeared to be galaxies although at $m > 23$ mag the star/galaxy separation remains uncertain. According to Windhorst et al. (2011) the fraction of stars is $\lesssim$10 and $\lesssim$1 per cent at $g \approx 23$ and 26 mag, respectively (see Appendix B1). In column 8 of Table 4 we give the contribution by all objects in the slit area in units of 10^{-9} erg cm^{-2} s^{-1} sr^{-1} Å^{-1} . Only a few per cent of this will be due to stars and we interpret it as the EBL contribution by the galaxies in the covered magnitude interval, given in column 7. The magnitude range varies from field to field with the bright and faint end values between 21.9–24.0 and 24.3–26.8 mag, respectively. The galaxy contributions for the 'Master' spectra areas vary from 0.40 to 0.58 $\times 10^{-9}$ erg cm^{-2} s^{-1} sr^{-1} Å^{-1} , with a mean of 0.51 $\times 10^{-9}$ erg cm^{-2} s^{-1} sr^{-1} Å^{-1} . For the 'Secondary' spectra fields the corresponding numbers are 0.29–1.11, with a mean of 0.54 $\times 10^{-9}$ erg cm^{-2} s^{-1} sr^{-1} Å^{-1}.

These numbers agree closely with the EBL contribution of 0.49 $\times 10^{-9}$ erg cm^{-2} s^{-1} sr^{-1} Å^{-1} for the magnitude interval of 22–27 mag, as estimated from galaxy count data in the *Hubble Space Telescope* (*HST*) *F*435*W* band by Driver et al. (2016, their table 3). We conclude that our total EBL intensity of $I_{\rm EBL} = 2.9 \pm 1.1\ 10^{-9}$ erg cm^{-2} s^{-1} sr^{-1} Å^{-1} includes a contribution of ∼0.5 $\times 10^{-9}$ erg cm^{-2} s^{-1} sr^{-1} Å^{-1} by galaxies in the magnitude interval of ∼22–26.5 mag.

4.2 Comparison with the integrated light of galaxies

We show in Fig. 6 a selection from UV to NIR (0.1–5 μm) of direct EBL measurements and upper and lower limits (colour symbols and lines), as well as lower limits set by the integrated galaxy light (IGL) from galaxy counts as derived by Driver et al. (2016) (black symbols). The EBL values from this paper are shown as the red solid square with 1σ error bars at 400 nm and as 2σ upper limits at 430 and 520 nm. For references see the figure legend.

When comparing our total EBL value at 400 nm with the IGL from galaxy counts one should take into account the magnitude limits of galaxies included in each case. As stated above, our EBL values exclude galaxies brighter than $B \approx 22$ mag whereas the

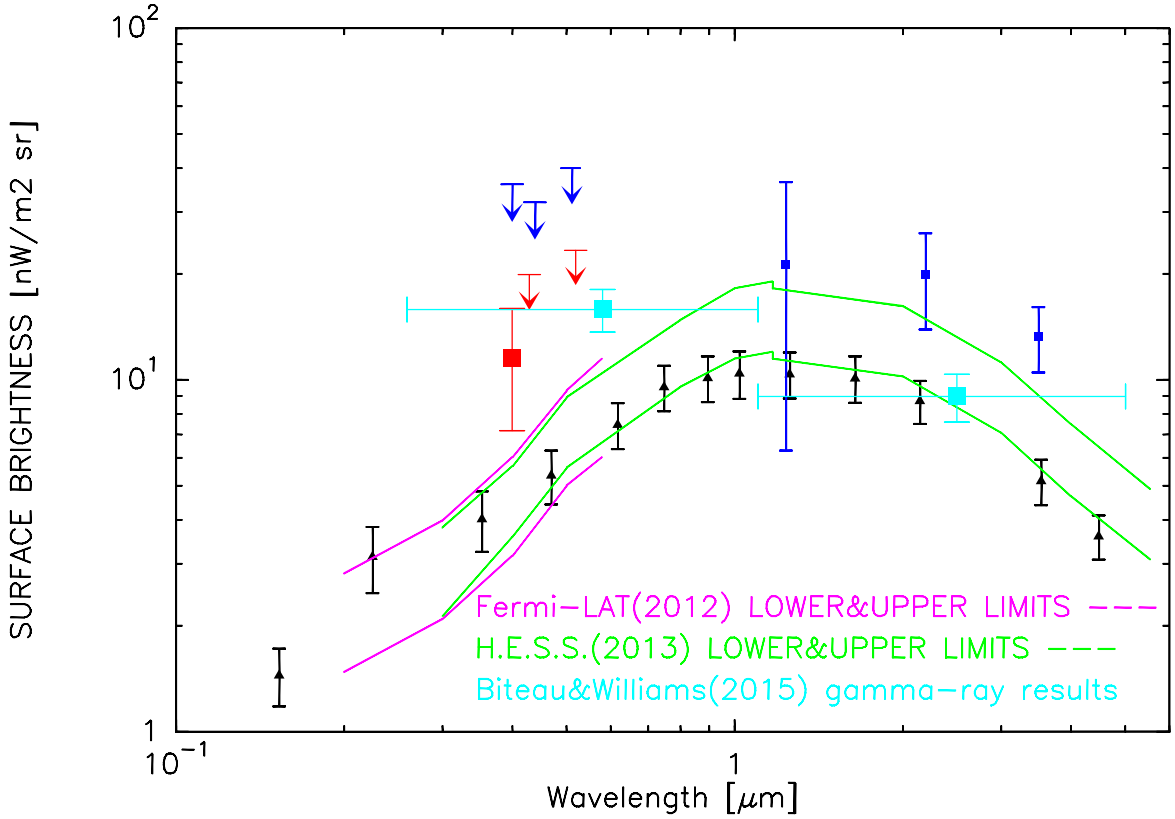

Figure 6. Selection of EBL measurements, upper and lower limits. *IGL*: 0.15–4.5 μm, Driver et al. (2016), black triangles. *Photometric EBL measurements and upper limits*: this paper: red square with 1σ error bars at 400 nm and 2σ upper limits at 430 and 520 nm; dark blue squares and arrows: 0.40 μm, Mattila (1990); 0.44 μm, Toller (1983); 0.5115 μm, Dube, Wickes & Wilkinson (1979), the latter three according to re-discussion in Leinert et al. (1998); 1.25, 2.2 and 3.6 μm, Levenson, Wright & Johnson (2007). *Results from gamma-ray attenuation:* upper and lower limits between 0.20–0.58 μm from *Fermi*-LAT (Ackermann et. al. 2012), magenta lines; between 0.30 and 5.5 μm from H.E.S.S. (H.E.S.S. Collaboration 2013), green lines; results of Biteau & Williams (2015) are shown as light blue crosses.

extrapolated eIGL values of Driver et al. (2016) cover the whole magnitude range, including extrapolations below $m \approx 10$ and above $m \approx$28–30 mag in optical bands from *u* to *h*. Using their table 3 one can estimate that galaxies with $g \leq$22 mag contribute $\sim$0.52 10^{-9} erg cm^{-2} s^{-1} sr^{-1} Å^{-1} of the total IGL of 1.14 $\pm$ 0.2 10^{-9} erg cm^{-2} s^{-1} sr^{-1} Å^{-1}. Thus the IGL contribution to be compared with our EBL measurement is $I_{\rm IGL}(g \geq 22^{\rm m}) = 0.62 \pm 0.2\ 10^{-9}$ erg cm^{-2} s^{-1} sr^{-1} Å^{-1} . On the other hand, if we include the bright-galaxy contribution for $g \leq 22$ mag, to our measured EBL value it will be increased to $I_{\rm EBL} = 3.5\ 10^{-9}$ erg cm^{-2} s^{-1} sr^{-1} Å^{-1} .

4.2.1 Cosmic variance and galaxy counts

We are able to check directly whether the L 1642 EBL fields are abnormal in terms of IGL using the direct imaging of the OFF fields described in Section 4.1. The photometric catalogues of the fields were cleaned of stars with the help of the SExtractor CLASS parameter (though the star contribution is significant only at $B < 22$, see Windhorst et al. 2011) and also of obvious artefacts and edge effects. The resulting *B*-band galaxy counts per deg^2 and 0.5 mag bin, averaged over the seven fields, are shown in Fig. 7. The counts from the shallower images, the Pos25 and Pos32 fields, are included only for $B \leq 24$ mag. The counts are not completeness corrected. For comparison we also show recent wide-field galaxy counts adopted from a large compilation of multiwavelength data by Driver et al. (2016). The points shown are *g*-band counts from GAMA and COSMOS/G10 surveys as described therein, we have merely shifted them using an average $B - g = 0.6$ mag conversion (Fukugita et al. 1996). The galaxy counts in our fields down to $B \sim 26$ mag thus appear totally normal and consistent with wide field galaxy counts.

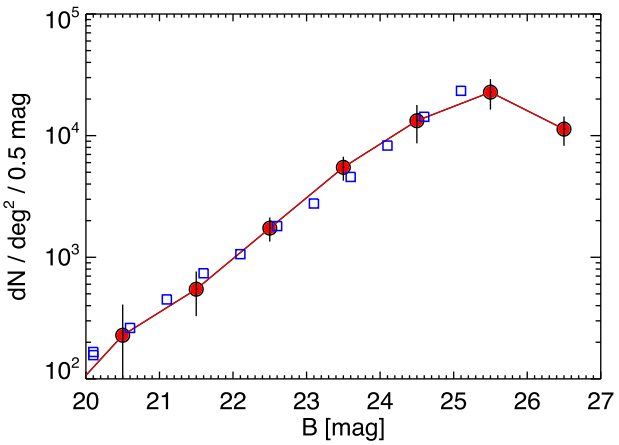

Figure 7. The red circles show the average galaxy number counts in the OFF fields, the error bars depict the standard deviation between counts of the seven separate fields. The counts are not completeness corrected, and the incompleteness is obvious at $B > 26$ mag. The blue squares show the *g*-band GAMA and G10 galaxy counts adopted from Driver et al. (2016), using an average $B = g + 0.6$ mag conversion.

The error bars in Fig. 7 are the standard deviations of counts between the fields, the nominal Poissonian errors within a field are in fact much smaller. The scatter reflects the cosmic variance. For the size (0.0126 deg^2) of our OFF fields we expect the cosmic variance to be of the order of 15–20 per cent (Driver & Robotham 2010), consistently with our results.

Finally, we note that there is a galaxy cluster, Abell 496, just north of the L 1642 area. One of our OFF positions, Pos18, is at the projected distance of 36.5 arcmin from the cD galaxy at the cluster centre. This corresponds to 1.63 Mpc at the cluster distance of 153.5 Mpc. While Pos18 shows one of the two highest galaxy counts of the seven fields examined, the difference is well within the scatter, the cosmic variance. An upper limit to the diffuse intra-cluster light contribution from Abell 496 can be estimated from the survey by Gonzalez, Zabludoff & Zaritsky (2005) of 24 clusters having a bright central galaxy with diffuse cD envelope. In this sample the highest diffuse light signal at large radii (up to ∼400 kpc) was for Abell 2984. Extrapolated to the projected distance of 1.63 Mpc and assuming a $B - I$ colour index of ≥2 mag it gives a B-band upper limit of ≤0.01 10^{-9} erg cm^{-2} s^{-1} sr^{-1} Å^{-1}. Photoelectric photometry of intra-cluster light in Abell 496 by Schnur & Mattila (1979) gave an upper limit of $\lesssim 2\ 10^{-9}$ erg cm^{-2} s^{-1} sr^{-1} Å^{-1} at the projected radial distance of 270–600 kpc. Adopting the radial gradient of Abell 2984 this extrapolates for 1.63 Mpc to $\lesssim$0.2 10^{-9} erg cm^{-2} s^{-1} sr^{-1} Å^{-1}. We conclude that Abell 496 does not have a measurable effect on our analysis. The contribution by Abell 496 can also be considered as a natural ingredient in the cosmic variance; in an area of ∼4° × 4° as covered by our OFF positions there normally exists, by chance, one major Abell cluster.

4.3 Comparison with EBL from gamma-ray attenuation measurements

The intergalactic radiation density has been derived from gamma-ray attenuation measurements of blazars by ground based Cerenkov telescopes, e.g. H.E.S.S., MAGIC and VERITAS, sensitive in the 0.2–20 TeV (VHE) range, as well as by the Large Area Telescope (LAT), aboard the *Fermi* satellite, sensitive in the 1–500 GeV (HE) range. Results based on extensive data sets from *Fermi*-LAT (Ackermann et. al. 2012) and H.E.S.S. (H.E.S.S. Collaboration 2013) are shown in Fig. 6 as upper and lower boundaries to the allowed range of EBL values. Similar results have been published by the MAGIC collaboration (Ahnen et al. 2016). *Fermi*-LAT probes with high sensitivity the EBL photon energy range from UV to optical ($\lambda \approx$ 200–600 nm) while the ground-based VHE telescopes cover the wider range from optical to FIR, $\lambda \approx$ 0.3–100 μm.

As can be seen from Fig. 6 the above-mentioned gamma-ray attenuation results agree with the IGL values from galaxy counts but they do allow a modestly higher (by up to $\lesssim$ 70 per cent) EBL intensity as well. The good agreement of spectral shapes is, however, a direct result of the underlying assumption of an IGL-like template spectrum: the EBL spectrum template comes from a model that is obtained by summing up empirically constrained galaxy populations spectra, see e.g. Franceschini, Rodighiero & Vaccari (2008) and Domínguez et al. (2013). The observed gamma-ray optical depths are fit to optical depths predicted by EBL spectral models, with a normalization factor as the only free parameter. Thus, the derived EBL spectrum will closely follow the spectrum of the IGL.

The interaction of gamma-rays versus optical and infrared EBL photons has a very broad wavelength response function, with the kernel covering roughly a decade of the EBL spectrum (Biteau & Williams 2015). Therefore, the intensity maximum at ∼1 μm dominates the normalization factor over the whole UV–NIR range

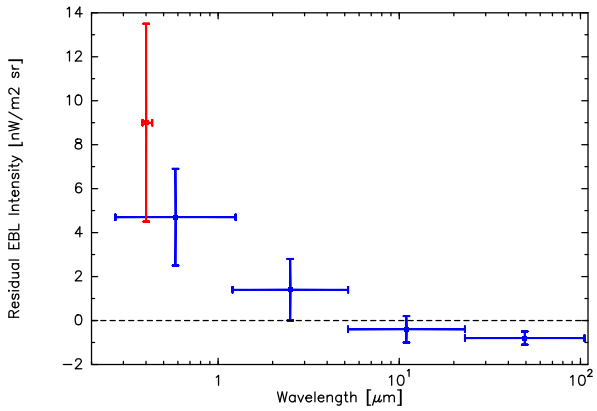

Figure 8. EBL residual values after subtraction of the IGL contribution as given in Driver et al. (2016). The four data points in blue have been adopted from fig. 4 of Biteau & Williams (2015) and are based on gamma-ray absorption measurements. The point in red is from this study.

0.2–5 μm and it will be difficult, if not impossible, to detect deviations from the IGL-like spectral shape using the 'model template approach'.

Recently, Biteau & Williams (2015) have taken a more general approach. They abstain from an a priori assumption on constraining the EBL spectrum with the IGL-like spectrum shape. Using gamma-ray observations only they were able to derive a 'free-standing' EBL spectrum that covered the 0.2–100 μm range by coarse binning, with four spectral elements with widths of approximately half a decade. Two of these spectral elements fall into the wavelength range displayed in Fig. 6 and they are shown as light blue crosses. The horizontal bars indicate the wavelength coverages of the bins, 0.26–1.2 and 1.2–5.2 μm, respectively.

Biteau & Williams (2015) have compared their EBL values with appropriately weighted IGL mean values in the four bins. While a good individual and overall agreement was found for the three bins at 1.2–5.2, 5.2–23 and 23–103 μm, the bin at 0.26–1.2 μm showed an excess of 4.7 ± 2.2 nW m^{-2} sr^{-1}. This excess over the IGL value, as well as over the *Fermi*-LAT and H.E.S.S. EBL values, is also well demonstrated by Fig. 6.

To compare with our EBL measurement we note that while the gamma-ray-based EBL value of 15.9 ± 2.2 nW m^{-2} sr^{-1} for the bin 0.26–1.2 μm corresponds to the total EBL, our EBL measurement at 0.4 μm does not include the contribution of the bright galaxies with $g \lesssim$22 mag. Including that contribution, our EBL value increases from 11.6 ± 4.4 nW m^{-2} sr^{-1}, as shown in Fig. 6, to 13.6 ± 4.5 nW m^{-2} sr^{-1}, which is in good agreement with the gamma-ray value of Biteau & Williams (2015). Furthermore, our total EBL value is in excess over the IGL value of Driver et al. (2016) at 0.4 μm by 9.0 ± 4.5 nW m^{-2} sr^{-1}.

We show in Fig. 8, in accordance to fig. 4 of Biteau & Williams (2015), our EBL excess value together with their four gamma-ray-based residual values. It can be seen that our excess value, while agreeing within the error limits with the 0.26–1.2 μm gamma-ray-based value, suggests an even larger excess at 0.4 μm.

In conclusion, our result that the EBL intensity at 400 nm exceeds the IGL from galaxy counts is supported by the Biteau & Williams (2015) EBL value, determined by the independent method of gamma-ray absorption.

4.4 Optical EBL in context of other wavelengths

The galaxies, intergalactic stars or any other light sources that give rise to the optical EBL will contribute to the background light also in

the adjacent UV and NIR wavelength bands. We will briefly review the recent results in these bands and their relevance for the optical EBL.

In the near ($\lambda \approx 150$ nm) and far-ultraviolet ($\lambda \approx 230$ nm) some of the large foreground sky components, e.g. the ZL, that plague optical EBL measurements are absent or much reduced. However, other difficulties appear, see e.g. Murthy (2009, 2014a,b) for a review. The *Galaxy Evolution Explorer (GALEX)* (Martin et al. 2005) has recently provided a comprehensive survey of the near (NUV) and far-ultraviolet (FUV) background, covering ∼75 per cent of the sky. Among the other surveys, Schiminovich et al. (2001) have covered a large fraction of sky at 174 nm in the *NUVIEWS* rocket experiment. The minimum sky brightness seen by *GALEX* towards the North and South Galactic Poles was ∼300–400 (FUV) and ∼600 photons cm^{-2} s^{-1} sr^{-1} Å^{-1} (NUV) (see Hamden, Schiminovich & Seibert 2013; Murthy et al. 2017). While these values still contain airglow as 'likely the dominant contributor' (Hamden et al. 2013) they can be used as upper limits to the EBL: $I_{\rm EBL}(\lambda) \lesssim 6-8$ and $\lesssim$12 nW m^{-2} sr^{-1} in the FUV and NUV band, respectively. These values are by a factor of ∼4 higher than the corresponding IGL values as displayed in Fig. 6.

Using a model for the distribution of dust and stellar light sources and adopting likely scattering parameters for the grains Murthy et al. (2017) estimated the scattered light from dust to be ∼1.2–1.8 (FUV) and ∼1 nW m^{-2} sr^{-1} (NUV). Schiminovich et al. (2001) estimated from their *NUVIEWS* data an EBL intensity of 4 ± 2 nW m^{-2} sr^{-1} at 174 nm. We conclude that the EBL estimates at FUV and NUV do allow an EBL contribution by at least two times as large as the IGL derived from galaxy counts, and are in this respect compatible with the EBL excess at 400 nm found in this paper.

Henry et al. (2015) have presented a different interpretation for the ∼300 photons cm^{-2}s^{-1} sr^{-1}Å^{-1} isotropic component of the *GALEX* FUV sky: they argue that most of it is not due to EBL but is 'of unknown (but Galactic) origin'.

The diffuse NIR background sky brightness has been studied by several groups using the *COBE* Diffuse Infrared Background Experiment (DIRBE) data in combination with the 2MASS star catalogue (see Dwek, Arendt & Krennrich 2005; Levenson et al. 2007; Sano et al. 2015 for reviews), the *AKARI* InfraRed Camera (Tsumura et al. 2013) and the *IRTS* Near Infrared Spectrometer (Matsumoto et al. 2005, 2015). Most of these results are consistent, within their large error bars, with the values as shown in Fig. 6 at 1.25, 2.2 and 3.6 μm according to the DIRBE–2MASS analysis of Levenson et al. (2007). The consensus, shared also by the TeV gamma-ray absorption results (Section 4.4 and Figs 6 and 8), appears to be that the NIR EBL does not exceed the IGL by more than a factor of 2.

Matsumoto et al. (2005), however, using their *IRTS* data have announced and Matsumoto et al. (2015) repeated the claim for detection of an excess emission of up to six times as large as the IGL at $\lambda = 1-2$ μm. A large excess has also been found by Sano et al. (2015) at 1.25 μm and by Matsuura et al. (2017) at 1−1.7 μm. It has been pointed out by e.g. Dwek et al. (2005) and Mattila (2006) that a likely explanation for the excess found in Matsumoto et al. (2005) is the insufficient subtraction of Zodiacal Light. Besides the ZL also the DGL introduces substantial uncertainty, especially at the shorter NIR wavelengths, into all these results.

Because of the persistent problems caused by the ZL the attention has turned towards the NIR sky fluctuations (see e.g. Kashlinsky et al. 2005, 2012; Matsumoto et al. 2011; Cooray et al. 2012). Recently Zemcov et al. (2014), using the Imager instrument of the *Cosmic Infrared Background Experiment*, found in the autocorrelation spectra of the fluctuations at 1.1 and 1.6 μm evidence for an excess power at angular scales $l = \pi/\theta < 5000$ (angular separations $\theta > 4.3$ arcmin). When interpreted as diffuse light from galaxy clusters and groups (jointly called intra-halo light, IHL), the modelling (Cooray et al. 2012) of this fluctuation excess lead them to conclude that the IHL contributes to the *mean* EBL (i.e. the 'dc component') at 1.1 and 1.6 μm 0.7 and 1.3 times as much light as the IGL from the galaxy counts. The interpretation has been challenged, however, by Yue, Ferrara & Salvaterra (2016) and Mitchell-Wynne et al. (2016) who suggest that most of these observed large-angular-scale fluctuations are due to the foreground DGL.

We conclude that direct photometric measures, both in the UV (100–300 nm) and NIR (1−5 μm), are compatible with an extra EBL component beyond the IGL from the galaxy counts of roughly the same amount as the IGL itself. However, the TeV gamma-ray absorption measurements, especially according to Biteau & Williams (2015), seem to exclude any substantial NIR excess (see Section 4.3 and Figs 6 and 8) while they support an optical excess, such as found in this paper.

4.5 Possible sources of background light from Milky Way halo and outside of galaxies

A survey for light sources that could explain the observed EBL excess over the IGL is presented in Appendix B. Possible light sources that are *known* to exist include light from Milky Way halo, from the outskirts of galaxies, or from intergalactic stars in galaxy clusters and groups. The contribution of such light sources may in certain objects or environments be very substantial, e.g. the intergalactic stars contribute up to 40 per cent of the luminosity of some clusters or groups. However, none of these sources are capable of explaining a substantial increase of the overall mean EBL beyond the IGL as derived from galaxy counts. Because of Lyman line and continuum absorption the redshift range of light sources contributing to sky brightness at $\lambda \lesssim 450$ mm is limited to redshifts $z \lesssim 3.5$. Contributions by primordial objects such as Population III stars or direct-collapse black holes are thus excluded. Light from hypothetical decaying dark matter particles, such as axions, remains an open field.

5 SUMMARY AND CONCLUSIONS

This paper is based on the results of Paper I (Mattila et al. 2017) where we have presented in the area the high-galactic-latitude dark cloud L 1642 spectrophotometric surface brightness observations performed with VLT/FORS at ESO/Paranal. Spectra for several transparent sightlines were observed *differentially* relative to the opaque core of the cloud. Because the transparent and opaque positions have been observed with exactly the same instrumental setup and in rapid time sequence no special requirements arised for *absolute* calibration accuracy. This is a decisive advantage as compared with those projects which derive the EBL as a (small) difference between two, ∼20–100 times larger, surface brightness signals measured by different telescopes and different techniques, requiring an extremely high *absolute* calibration accuracy, separately for each.

The dark cloud offers an opaque screen towards which the EBL is close to zero. However, it produces also a foreground component, the scattered light from the dust. This, the only, foreground contaminant is an order of magnitude weaker than Zodiacal Light and ISL, the main contaminants in the EBL measurement methods of Bernstein, Freedman & Madore (2002a) and Matsuoka et al. (2011). We have accomplished the separation of the scattered light at the opaque position using the different spectral characteristics of the scattered Galactic starlight and the EBL spectrum. As template for

the scattered starlight we have made use of the observed spectrum at semitransparent positions in the cloud.

The main results and conclusions of this paper can be summarized as follows:

(1) The EBL has been detected at 400 nm at 2.6σ level. At 520 nm we have set a significant upper limit.

(2) The EBL value at 400 nm is

$2.9 \pm 1.1\ 10^{-9}$ erg cm^{-2} s^{-1} sr^{-1} Å^{-1} +20 per cent/−16 per cent

or

11.6 ± 4.4 nW m^{-2} sr^{-1} +20 per cent/−16 per cent, which is $\gtrsim$2 times as high as the IGL, even if possible contributions by galaxy haloes to the IGL are included.

(3) The 2σ upper limit to EBL at 520 nm is

$\leq 4.5\ 10^{-9}$ erg cm^{-2} s^{-1} sr^{-1} Å^{-1} +20 per cent/−16 per cent or

≤ 23.4 nW m^{-2}sr^{-1} +20 per cent/−16 per cent.

(4) Our EBL value at 400 nm is in good agreement with the indirect measurement via gamma-ray attenuation of blazars, presuming that the attenuation analysis has been performed, like in Biteau & Williams (2015), without a restrictive presupposed EBL spectral template form.

(5) No diffuse light sources, such as light from Milky Way halo, intra-cluster or intra-group stars, or from decaying elementary particles appear capable of explaining the observed EBL excess over the IGL.

ACKNOWLEDGEMENTS

This research has made use of the Image and Catalogue Archive operated by the United States Naval Observatory, Flagstaff Station (http://www.nofs.navy.mil/data/fchpix/).

The Digitized Sky Surveys were produced at the Space Telescope Science Institute under U.S. Government grant NAG W-2166. The images of these surveys are based on photographic data obtained using the Oschin Schmidt Telescope on Palomar Mountain and the UK Schmidt Telescope. The plates were processed into the present compressed digital form with the permission of these institutions. We thank Dr. Simon Driver for valuable comments concerning galaxy counts and photometry and the anonymous referee for useful comments of general nature. KM and KL acknowledge the support from the Research Council for Natural Sciences and Engineering (Finland); PV acknowledges the support from the National Research Foundation of South Africa.

This research is based on observations collected at the European Organisation for Astronomical Research in the Southern Hemisphere, under ESO programmes 072.A-0208(A), 082.A-0421(A) and 086.A-0201(A).

REFERENCES

Ackermann M. et al., 2012, Science, 338, 1190
Adami C. et al., 2005, A&A, 429, 39
Adami C. et al., 2016, A&A, 592, A7
Ahnen M. L. et al., 2016, A&A, 590, A24
Aller L. H., 1984, ASSL, 112, 102
Bartunov O. S., Tsvetkov D. Y., Pavlyuk N. N., 2007, Highlights Astron., 14, 316 (The complete version of this paper is available at http://www.sai.msu.su/sn/pubs/sncatdistr.pdf)
Benítez N. et al., 2004, ApJS, 150, 1
Bernstein R. A., 2007, ApJ, 666, 663
Bernstein R. A., Freedman W. L., Madore B. F., 2002a, ApJ, 571, 56
Bernstein R. A., Freedman W. L., Madore B. F., 2002b, ApJ, 571, 107
Bertin E., Arnouts S., 1996, A&AS, 117, 393
Biteau J., Williams D. A., 2015, ApJ, 812, 60
Brandt T. D., Draine B. T., 2012, ApJ, 744, 129
Bruzual G., Charlot S., 2003, MNRAS, 344, 1000
Burke C., Collins C. A., Stott J. P., Hilton M., 2012, MNRAS, 425, 2058
Burke C., Hilton M., Collins C., 2015, MNRAS, 449, 2353
Cardelli J. A., Clayton G. C., Mathis J. S., 1989, ApJ, 345, 245
Ciardullo R., Mihos J. C., Feldmeier J. J., Durrell P. R., Sigurdsson S., 2004, in Duc P.-A., Braine J., Brinks E., eds, Proc. IAU Symp. 217, The Systematics of Intracluster Starlight. Astron. Soc. Pac., San Francisco, p. 88
Cooray A. et al., 2012, Nature, 490, 514
Da Rocha C., Mendes de Oliveira C., 2005, MNRAS, 364, 1069
Davies L. J. M. et al., 2015, MNRAS, 447, 1014
Disney M., Lang R., Ott J., 2016, MNRAS, preprint (arXiv:1603.02590)
Domínguez A., Finke J. D., Prada F., Primack J. R., Kitaura F. S., Siana B., Paneque D., 2013, ApJ, 770, 77
Doyle M. T. et al., 2005, MNRAS, 361, 34
Driver S. P., 1999, ApJ, 526, L69
Driver S. P., Robotham A. S. G., 2010, MNRAS, 407, 2131
Driver S. P., Liske J., Cross N. J. G., De Propris R., Allen P. D., 2005, MNRAS, 360, 81
Driver S. P. et al., 2016, ApJ, 827, 108
Dube R. R., Wickes W. C., Wilkinson D. T., 1979, ApJ, 232, 333
Dwek E., Arendt R. G., Krennrich F., 2005, ApJ, 635, 784
Eke V. R., Baugh C. M., Cole S., Frenk C. S., King H. M., Peacock J. A., 2005, MNRAS, 362, 1233
Flynn C., Holmberg J., Portinari L., Fuchs B., Jahreiß H., 2006, MNRAS, 372, 1149
Franceschini A., Rodighiero G., Vaccari M., 2008, A&A, 487, 837
Fukugita M., Ichikawa T., Gunn J. E., Doi M., Shimasaku K., Schneider D. P., 1996, AJ, 111, 1748
Gal-Yam A., Maoz D., Guhathakurta P., Filippenko A. V., 2003, AJ, 125, 1087
Gong Y., Cooray A., Mitchell-Wynne K., Chen X., Zemcov M., Smidt J., 2016, ApJ, 825, 104
Gonzalez A. H., Zabludoff A. I., Zaritsky D., 2005, ApJ, 618, 195
Graham M. L., Sand D. J., Zaritsky D., Pritchet C. J., 2015, ApJ, 807, 83
Guennou L. et al., 2012, A&A, 537, A64
H.E.S.S. Collaboration 2013, A&A 550, A4
Hamden E. T., Schiminovich D., Seibert M., 2013, ApJ, 779, 180
Haynes M. P. et al., 2011, AJ, 142, 170
Henry R. C., Murthy J., Overduin J., Tyler J., 2015, ApJ, 798, 14
Hodges-Kluck E., Bregman J. N., 2014, ApJ, 789, 131
Impey C., Bothun G., 1989, ApJ, 341, 89
Kapferer W., Schindler S., Knollmann S. R., van Kampen E., 2010, A&A, 516, A41
Kashlinsky A., Arendt R. G., Mather J., Moseley S. H., 2005, Nature, 438, 45
Kashlinsky A., Arendt R. G., Ashby M. L. N., Fazio G. G., Mather J., Moseley S. H., 2012, ApJ, 753, 63
Koda J., Yagi M., Yamanoi H., Komiyama Y., 2015, ApJ, 807, L2
Le Borgne J.-F. et al., 2003, A&A, 402, 433
Laureijs R. J., Mattila K., Schnur G., 1987, A&A, 184, 269
Lehtinen K., Mattila K., 2013, A&A, 549, A91
Leinert C. et al., 1998, A&AS, 127, 1
Levenson L. R., Wright E. L., Johnson B. D., 2007, ApJ, 666, 34
Longair M. S., 1995, in Binggeli B., Buser R., eds, Saas-Fee Advanced Course, Vol. 23, The Deep Universe. :Springer, Berlin, p. 317
Loys de Chéseaux J.-P., 1744, Traité de la comète qui apparut en décembre 1743, Lausanne, p. 223
McGaugh S., 1994, Nature, 367, 538
McGee S. L., Balogh M. L., 2010, MNRAS, 403, L79
Martin D. C. et al., 2005, ApJ, 619, L59
Matsumoto T. et al., 2005, ApJ, 626, 31
Matsumoto T. et al., 2011, ApJ, 742, 124
Matsumoto T., Kim M. G., Pyo J., Tsumura K., 2015, ApJ, 807, 57
Matsuoka Y., Ienaka N., Kawara K., Oyabu S., 2011, ApJ, 736, 119
Matsuura S. et al., 2017, ApJ, 839, 7
Mattila K., 1971, A&A, 15, 292
Mattila K., 1976, A&A, 47, 77
Mattila K., 1980a, A&A, 82, 373

Mattila K., 1980b, A&AS, 39, 53
Mattila K., 2006, MNRAS, 372, 1253
Mattila K., 1990, in Bowyer S.A., Leinert Ch., eds, Proc. IAU Symp. 139, Galactic and Extragalactic Background Radiation. Kluwer, Dordrecht, p. 257
Mattila K., Lehtinen K., Väisänen P., von Appen-Schnur G., Leinert C., 2017, MNRAS, 470, 2133 (Paper I)
Mihos C., 2015, IAUGA, 22, 2247903
Mihos J. C., Harding P., Feldmeier J., Morrison H., 2005, ApJ, 631, L41
Mitchell-Wynne K., Cooray A., Xue Y., Luo B., Brandt W., Koekemoer A., 2016, ApJ, 832, 104
Murthy J., 2009, Ap&SS, 320, 21
Murthy J., 2014a, ApJS, 213, 32
Murthy J., 2014b, Ap&SS, 349, 165
Murthy J., Akshaya M. S., Ravichandran S., Henry R. C., Overduin J., 2017, MNRAS, preprint (arXiv:1701.07644)
Olbers H. W. M., 1823, Astronomisches Jahrbuch 1826, hrsg. von J.E. Bode, p. 110
Osterbrock D. E., Ferland G. J., 2006, Astrophysics of Gaseous Nebulae and Active Galactic Nuclei, 2nd edn. University Science Books, Sausalito, CA, p. 73
Overduin J. M., Wesson P. S., 2004, Phys. Rep., 402, 267
Overduin J. M., Wesson P. S., 2008, Light/Dark Universe. World Scientific, Singapore
Presotto V. et al., 2014, A&A, 565, A126
Rudick C. S., Mihos J. C., Harding P., Feldmeier J. J., Janowiecki S., Morrison H. L., 2010, ApJ, 720, 569
Sano K., Kawara K., Matsuura S., Kataza H., Arai T., Matsuoka Y., 2015, ApJ, 811, 77
Schiminovich D., Friedman P. G., Martin C., Morrissey P. F., 2001, ApJ, 563, L161
Schnur G., Mattila K., 1979, MitAG, 45, 196
Seon K.-i., Witt A. N., Shinn J.-h., Kim I.-j., 2014, ApJ, 785, L18
Toller G. N., 1983, ApJ, 266, L79
Totani T., Yoshii Y., Iwamuro F., Maihara T., Motohara K., 2001, ApJ, 550, L137
Tsumura K., Matsumoto T., Matsuura S., Sakon I., Wada T., 2013, PASJ, 65, 121
van Dokkum P. G., Abraham R., Merritt A., Zhang J., Geha M., Conroy C., 2015, APJ, 798, L45
Väisänen P., 1996, A&A, 315, 21
Wainscoat R. J., Cohen M., Volk K., Walker H. J., Schwartz D. E., 1992, ApJS, 83, 111
White P. M., Bothun G., Guerrero M. A., West M. J., Barkhouse W. A., 2003, ApJ, 585, 739
Windhorst R. A. et al., 2011, ApJS, 193, 27
Yue B., Ferrara A., Salvaterra R., 2016, MNRAS, preprint (arXiv:1601.02514)
Zemcov M. et al., 2014, Science, 346, 732
Zwicky F., 1951, PASP, 63, 61

SUPPORTING INFORMATION

Supplementary data are available at *MNRAS* online.

Table A1. Data for space distribution parameters of stars and spectral library (STELIB) stars used for the ISL synthetic spectrum.

Please note: Oxford University Press is not responsible for the content or functionality of any supporting materials supplied by the authors. Any queries (other than missing material) should be directed to the corresponding author for the article.

APPENDIX A: SYNTHETIC MODEL OF THE INTEGRATED STARLIGHT

Spectral synthesis is a common method in studies of stellar populations in external galaxies that are too distant to be resolved into individual stars (see e.g. Bruzual & Charlot 2003). We address the opposite problem: given the number densities and spatial distribution of the different types of stars and dust in the Solar neighbourhood what is the spectrum of the ISL in different directions of sky and for different vantage points of an observer off the Galactic plane. In addition to the ISL the Galactic surface brightness contains also the diffusely scattered starlight, the DGL. Since its spectrum is a copy of the ISL spectrum it does not influence the strengths of the spectral features (absorption lines, bands, discontinuities). Our calculation of the ISL spectrum between 370 and 600 nm follows the methods as presented in Mattila (1980a,b) with an update in Lehtinen & Mattila (2013).

A1 Galaxy model and stellar distribution parameters

A simple model of the Galactic structure is adopted in which stars and dust are distributed in plane-parallel layers. The effect of clumpy dust distribution is taken into account. Stars have been divided into 72 spectral groups covering the different parts of the HR-diagram. The division has been made according to the approach of Flynn et al. (2006) based on their analysis of the *Hipparcos* data base.[6] The spectral groups are combined under the following seven categories (see Table A1): *(i, ii)* Main Sequence (thin and thick disc), *(iii, iv)* Clump Stars (thin and thick disc), *(v, vi)* Old Giants (thin and thick disc), *(vii)* Young Giants. For each group Table A1 gives the mean absolute magnitude, M_V, the number density, $D(0)$, and stellar emission coefficient, $j_i(0)$, in the Galactic plane, $z = 0$, and the scaleheight h_z for a distribution of the form $D(z) = D(0)\mathrm{sech}(z/h_z)$. Because of the limited distance range of *Hipparcos* its coverage for the supergiants was sparse. We complemented this part by using the compilation of Wainscoat et al. (1992).

A2 Stellar spectral library

For the synthetic model of the 370–600 nm ISL spectrum we need a spectral library with good spectral type and wavelength coverage and a sufficient spectral resolution, corresponding to our observed spectra. The STELIB library (Le Borgne et al. 2003)[7] matches well these conditions. In order to choose the best template stars from the library for each of our stellar groups as given in Table A1 we have used besides the spectral classes and absolute magnitudes M_V also the colour indices $B - V$ and $V - I_c$ as selection criteria. In most cases a satisfactory match was possible. The STELIB catalogue numbers are given in column 9 of Table A1.

A3 Results

We have shown in fig. 2 of Paper I the resulting ISL spectrum, mean over the sky, for an observer located at 85 pc off the Galactic plane, corresponding to the estimated z-distance of the L 1642 cloud. In Fig. A1 we compare this ISL spectrum with the observed mean spectrum for positions 9 and 42, $\Delta I(\lambda)$(Pos9/42–OFF). At these positions the obscuration of the EBL is small and the spectral shape is only weakly influenced by dust. The observed spectrum is shown as black dots and the ISL model spectrum as the uppermost blue curve. It has been scaled by the factor $G_{\mathrm{sca}}(\lambda) = 0.225[1 - 1.0 \times 10^{-4}\,\mathrm{nm}^{-1}(\lambda - 500\,\mathrm{nm})]$ (see equation 6) to account for a slight bluening of the Pos9/42 spectrum w.r.t. the

[6] Drs. Flynn and Portinari kindly provided us with their results in detailed tabular form.
[7] http://www.ast.obs-mip.fr/article181.html

Table A1. Data for space distribution parameters of stars and spectral library (STELIB) stars used for the ISL synthetic spectrum. Column 3 gives the mean and columns 4–5 the range of absolute magnitude, M_V, of the spectral group; column 6 gives the number density, $D(0)$ and column 8 the stellar emission coefficient, $j_i(0)$, in units of $M_V = 0$ mag stars pc^{-3}, in the Galactic plane, $z = 0$; the scaleheight h_z for a distribution of the form $D(z) = D(0)\mathrm{sech}(z/h_z)$ is given in column 7; the last column gives the number in the STELIB library of the spectrum adopted as template for each spectral group. *The full table is available in the online version.*

No.	Sp class	M_V	M_V range		D_0	h_z	j_0	STELIB star no.
		mag	mag		stars pc^{-3}	pc	$M_V = 0$ mag stars pc^{-3}	
Main sequence, thin disc								
1	B0 V	−4.0	−4.20	−3.25	0.46E−06	56.	0.13E−04	23
2	B2 V	−2.45	−3.20	−1.85	0.34E−05	56.	0.32E−04	21
3	B5 V	−1.2	−1.80	−0.75	0.13E−04	56.	0.38E−04	94
4	B8 V	−0.25	−0.70	0.20	0.44E−04	57.	0.53E−04	124
5	A0 V	0.65	0.25	0.95	0.92E−04	68.	0.52E−04	163
6	A2 V	1.3	1.00	1.60	0.15E−03	82.	0.44E−04	152
7	A3–5 V	1.8	1.65	1.95	0.11E−03	92.	0.21E−04	149
...	...	...	...	...	...	...	...	...
72	M3–4 I–II	−5.79	−5.8	−5.8	0.13E−07	56.	0.27E−05	7

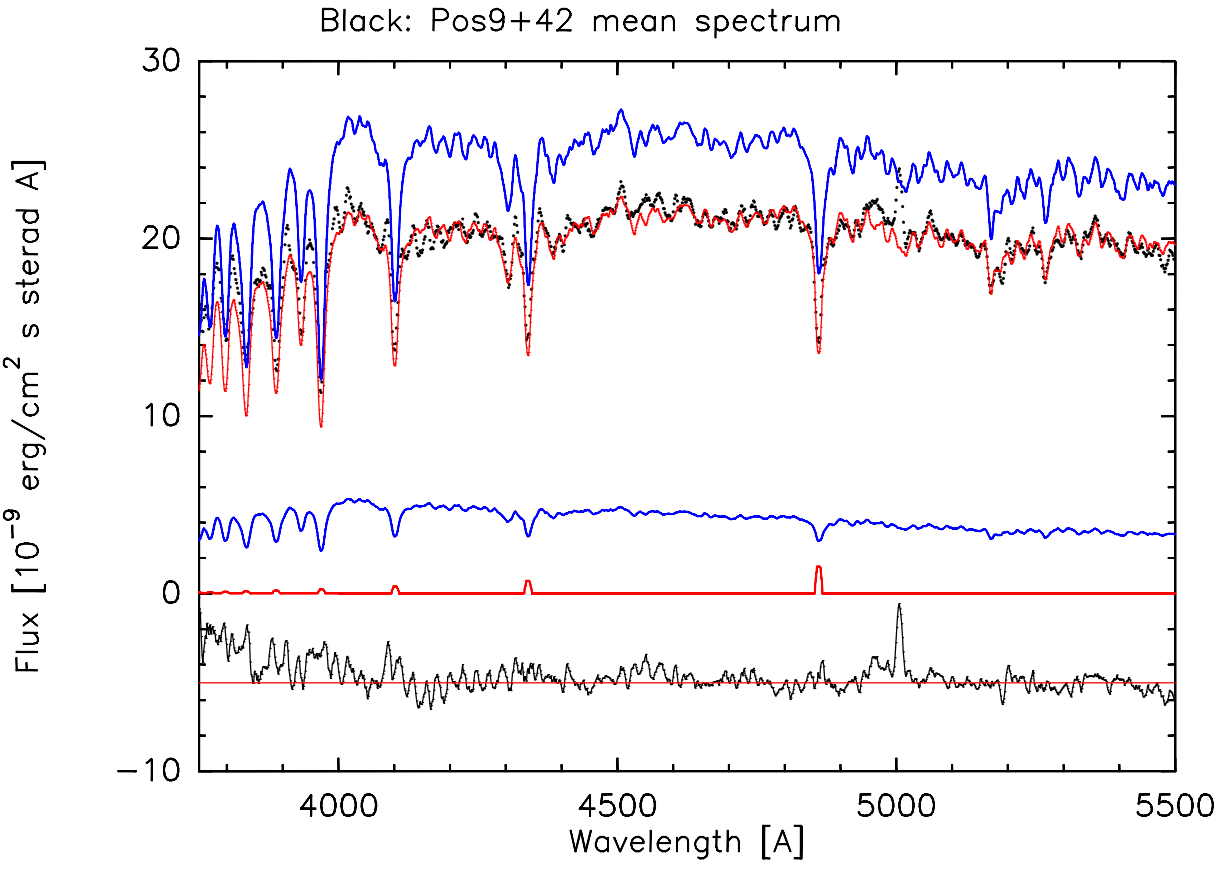

Figure A1. Comparison of the mean spectrum of the intermediate-opacity positions 9 and 42 with the synthetic ISL model spectrum (see Appendix A). The observed spectrum, $\Delta I(\lambda)$(Pos9/42–OFF), is represented as black dots. The ISL spectrum is shown as the uppermost blue line. The lower blue curve is the scattered light spectrum and the red line the ionized hydrogen emission spectrum for the OFF positions. The model fit is shown as the red curve superimposed on the observed spectrum. The residuals *observed minus model fit* are shown as the bottom-most black curve, with zero level shifted by -5×10^{-9} erg cm^{-2} s^{-1} sr^{-1} Å^{-1} . Notice that the large residual at 500.7 nm is due to the [O III] emission. See the text for details.

ISL spectrum. The OFF spectrum, calculated according to equation (7), is shown as the lower blue curve. The ON–OFF model fit, shown as the red curve, has been optimized for $\lambda > 400$ nm. The Balmer line emission in the OFF areas is shown in red with baseline at zero. It can be seen that while the overall fit is good for $\lambda > 400$ nm there is a substantial discrepancy with the 400 nm step size: this results in *observed minus model* values, shown as black line, deviating systematically upwards at $\lambda < 400$ nm, i.e. the ISL

model predicts a larger step at 400 nm than the observed one. Such a behaviour cannot be explained by an EBL contribution either: a residual EBL contribution would have an effect in the opposite direction.

Many of the ISL spectral structures, even at low levels, are recognized also in the scattered light spectrum. Notice, however, the emission line at 500.7 nm in the scattered light spectrum that is not present in the ISL; it originates from the all-sky ionized gas emission of [O III].

APPENDIX B: POSSIBLE SOURCES OF EBL BEYOND GALAXY COUNTS: MILKY WAY HALO, OUTSKIRTS OF GALAXIES, LOW SURFACE BRIGHTNESS GALAXIES, INTERGALACTIC STARS AND DECAYING DARK MATTER PARTICLES

B1 Unresolved starlight and light from the Milky Way halo

Sky background light as seen by an observer inside the Galaxy contains contributions from unresolved stars, diffuse emission from gas and scattered light from dust.

The light from unresolved stars in the *B* band can be estimated by using the deep *HST* Advanced Camera for Surveys (ACS) starcounts in the *F*435*W* filter band ($\lambda_c = 429.7$ nm) as presented by Windhorst et al. (2011) for the GOODS S field. At $m(F435W) = 20$ mag the number of stars is approximately equal to the galaxy numbers but, because of the shallow slope of the star counts $\mathrm{d}(\log N(m))/\mathrm{d}m \approx 0.065$, it drops at $m(F435W) = 27$ mag to ∼1 per cent of the galaxy counts. Using this slope to extrapolate the star counts beyond 27 mag we find that the integrated starlight for $m(F435W) \geq 25$ mag amounts to $I_{\rm ISL} \approx 0.0034 \times 10^{-9}$ erg cm^{-2} s^{-1} sr^{-1} Å^{-1} . The GOODS S field at $(l, b) = 224^\circ, -54^\circ$ is relatively close to the L 1642 field at $(l, b) = 210^\circ, -37^\circ$. Taking into account the different LOS lengths through the Galactic (roughly plane-parallel) star layer we estimate that $I_{\rm ISL}(B \geq 25$ mag) $\approx 0.0045 \times 10^{-9}$ erg cm^{-2} s^{-1} sr^{-1} Å^{-1} towards L 1642 and can be neglected in the further discussion.

Extended far-ultraviolet ($\lambda \approx 150$–250 nm) haloes have been observed around several edge-on late-type galaxies out to 5–10 kpc from the mid-plane (e.g. NGC 891, NGC 5907; see Hodges-Kluck & Bregman 2014; Seon et al. 2014). They have been ascribed to thick dust discs that scatter light from stellar discs of the galaxies. The existence of substantial amounts of dust in the Milky Way halo at, say $|z| > 2$ kpc, is not known. However, any such dust would be illuminated by an ISRF that has closely the same absorption line spectrum as the scattered light of the L 1642 cloud. Therefore, it will be largely eliminated by our spectral separation method as described in Section 2.

Gas emission from Milky Way halo is expected to be almost entirely in the form of line emission, mostly the hydrogen Balmer lines, plus a very weak continuum. They have been taken into account in the analysis as described in Section 2.1.3.

B2 Light from the outskirts of galaxies

Not all light of a galaxy is captured by fixed aperture or Kron standard photometry. The light loss from the outskirts of galaxies, i.e. galaxy wings, may be only partially compensated for by corrections towards 'total' magnitudes and this may lead to underestimates of the IGL. Totani et al. (2001) studied its influence via photometric modelling with reasonable assumptions on galaxy wings and other correction factors. They found that their 'best guess' IGL from all galaxies in the Universe was up to 80 per cent higher than the IGL from a simple integration of observed galaxy counts.

In a detailed analysis of the *HST Deep Field* (HDF) and their own EBL field Bernstein et al. (2002a) and Bernstein, Freedman & Madore (2002b) derived galaxy magnitudes using SExtractor Kron-type photometry with different Kron parameters $k = r/r_{\rm iso}$ (their isophotal magnitudes varied from 24.7 to 25.8 ST mag arcsec^{-2}). They found that at least 20 per cent of the flux of the faintest galaxies (i.e. within 4.5 mag of the detection limit) was contributed by galaxy wings at $r > 1.4 r_{\rm iso}$. Furthermore, using a method called 'ensemble photometry' they estimated that the true flux from $V > 23$ AB mag galaxies in the HDF can be almost twice as much as that recovered by standard photometric methods. Benítez et al. (2004) analysed the faint galaxy population in two early release science (ERS) fields of the *HST* ACS. They confirmed the claim of Bernstein et al. (2002a,b) of an up to 50 per cent loss of light of the faintest galaxies.

The galaxy photometry used by Driver et al. (2016) for their IGL values in the optical bands is, at the faint end, based on the *HST*/ACS ERS and the *Hubble Ultra Deep Field* (HUDF) observations that are deeper than the HDF data used by Bernstein et al. (2002a,b) and are, therefore, less vulnerable to effects of galaxy wings. While both the ACS ERS (Windhorst et al. 2011) and the HUDF photometry made use of a larger Kron factor, $k = 2.5$, than Bernstein et al. (2002a,b) the HUDF photometry was also otherwise designed to take better care of the galaxy-wing contribution. The galaxy counts from the two sets of data were in good agreement and agreed with the GAMA G10 data as well. This suggested that the galaxy wings do not have an effect of more than 20 per cent on the faint galaxy fluxes used in Driver et al. (2016), and the effect is rather likely at <10 per cent level (Driver, private communication, 2017).

As a simple test of consistency and as test of aperture size effects regarding faint galaxy photometry, we downloaded the HUDF frames[8] and ran our SExtractor photometry mentioned in Section 4.1 over the *B*-band image. We did this in two ways, first with a standard setup using 2.5 for the Kron parameter, and then doubling it to 5.0, essentially doubling most elliptical aperture sizes. Other parameters were fixed, the background being estimated in a 24-pixel thick annulus outside the apertures. We do find, as e.g. Benítez et al. (2004) indicate, that many galaxies *close to the detection limit* become significantly brighter when using the larger apertures. However, the systematic effect in our simple test is not nearly as large as 50 per cent for the light missed, but rather closer to 20 per cent. Moreover, when summing up all the sources in the field over the whole detected magnitude range, the missing light fraction is only 6 per cent.

Thus, while it well may be that significant amounts of light are missed in 'typical' galaxy photometric techniques, it might be difficult to imagine that those surveys where specific care is taken against such effects could still miss more than, say, 20 per cent of the total light because of the galaxy outskirts. Moreover, an obvious counter-argument for large fractions of missing light at the outskirts of galaxies is the absence of large SN populations in these areas. From the results of Bartunov, Tsvetkov & Pavlyuk (2007) one finds that only ∼5–7 per cent of the total number of SN events occur at radii $r = (1.4 - 4) r_{25}$.

[8] https://archive.stsci.edu/prepds/udf/

B3 Low surface brightness galaxies

Galaxies with very low surface brightness (LSBG) could escape detection altogether in galaxy counts, or their total brightness be significantly underestimated even if detected, due to various selection effects (e.g. McGaugh 1994). Hence it is in principle possible that these galaxies could contribute significantly to EBL while not adding to the integrated galaxy counts, even by a factor of two or more if suitable populations are constructed (e.g. Väisänen 1996). However, though such galaxies exist (e.g. Malin 1, the most famous case, Impey & Bothun 1989), deep optical surveys (e.g. Driver et al. 2005) or using radio/21-cm H I surveys as pin-pointers (e.g. Doyle et al. 2005; Haynes et al. 2011) over the past two decades have failed to detect significant populations of field LSBGs. In rich clusters, numerous LSBGs or ultra diffuse galaxies have recently been detected (e.g. Davies et al. 2015; Koda et al. 2015; van Dokkum et al. 2015) but their total contribution to the IGL remains small. The consensus appears to be that less than 20 per cent of additional light is contributed by the LSBGs to the IGL (e.g. Driver 1999; Driver et al. 2005).

Note however that Disney, Lang & Ott (2016) have recently argued that dim and/or dark galaxies might still be evading surveys if such galaxies were strongly clustered.

B4 Intra-cluster and intra-group light

Intra-cluster (ICL) and intra-group light, sometimes collectively also referred to as IHL (Cooray et al. 2012), is a well-established component among cosmic light sources. It originates from stars stripped off from galaxies in the cluster formation phase or in later interactions between galaxies or, perhaps, also from stars formed *in situ* in the intra-cluster gas (see e.g. Kapferer et al. 2010).

Diffuse light between the galaxies was first noted by Zwicky (1951) in deep photographs of the Coma Cluster. Wide-field CCD cameras have enabled deep surface brightness imaging of the intergalactic light in Coma (e.g. Adami et al. 2005), Virgo (e.g. Mihos et al. 2005; Rudick et al. 2010) and several other nearby and more distant clusters and galaxy groups (for a review, see Mihos 2015).

The fraction of intra-cluster light of the total cluster luminosity varies between 15 and 40 per cent for the nearby big clusters (Ciardullo et al. 2004). For clusters in the redshift range z ∼0.2–0.4 some studies (Burke, Hilton & Collins 2015) find that the ICL fractions are decreasing with redshift from ∼25 to $\lesssim$5 per cent while in others (Guennou et al. 2012; Presotto et al. 2014) the values are still high, ∼ 25 per cent, or even higher (Adami et al. 2016). From six clusters at redshifts of z ∼0.8–1.2 Burke et al. (2012) find ICL fractions of ∼1–5 per cent.

In galaxy groups the fraction of diffuse light varies even more strongly from undetectable in loose groups to ∼30–40 per cent in many compact groups (see e.g. White et al. 2003; Da Rocha & Mendes de Oliveira 2005).

The intra-cluster SN events account for $\lesssim$ 20 per cent of the SN rate for the clusters, in agreement with the estimates of the diffuse light fraction (Gal-Yam et al. 2003; Graham et al. 2015). For the intergalactic SN events in groups an upper limit of $\lesssim$32 per cent has been set by the fraction of apparently hostless Type Ia SNe (McGee & Balogh 2010).

Although the diffuse light fraction in individual clusters and dense groups may be high, up to 40 per cent, it is important to remember that rich clusters contribute only a few per cent of the total cosmic starlight while 80 per cent of the light comes from individual field galaxies or loose groups, like the Local Group, with luminosities $<10^{11}$ $L_{\odot}$ (Eke et al. 2005). Therefore, hardly more than 10 per cent is added to the integrated galaxy light by the contributions from ICL and intra-group starlight.

B5 Other sources of diffuse light

Because of Lyman line and continuum absorption the redshift range of light sources contributing to sky brightness at $\lambda \lesssim 450$ mm is limited to $z \lesssim 3.5$. Contributions by primordial objects such as Population III stars or direct collapse black holes are thus excluded.

Decaying or annihilating dark matter candidate particles, such as neutrinos, WIMPs and axions, have been proposed as possible sources of diffuse background radiation fields. On the other side, the EBL might qualify as an important discovery channel for the elusive dark matter particles; for a review, see Overduin & Wesson (2004, 2008) and the update in Henry et al. (2015). Recently, Gong et al. (2016) have discussed the possibility that the NIR background *fluctuations* could partly originate from decaying axions with mass around 4 eV, located mainly in the haloes of clusters and groups. None of the three particle species have been found to produce enough radiation to qualify as serious contributor to the *mean* intensity of the EBL in UV (Henry et al. 2015), optical or NIR (Gong et al. 2016) domain. Furthermore, axions and WIMPS should be strongly concentrated to the dark matter haloes of clusters, groups and individual galaxies. Even if some part of the diffuse intra-cluster, intra-group or galaxy halo diffuse light were caused by decaying particles, instead of stars, this would not change the amount of diffuse light as determined by the observations. Only a smoothly distributed diffuse light component, present also in the general field outside the clusters, could have escaped the observations.

This paper has been typeset from a TEX/LATEX file prepared by the author.